2012

Geodynamic Constraints on the Flow of Samoan-Plume Mantle into the Northern Lau Basin

Nathan Katsiaficas
Colby College

GEODYNAMIC CONSTRAINTS ON THE FLOW OF SAMOAN-PLUME MANTLE INTO THE NORTHERN LAU BASIN

Nathan Katsiaficas ‘12

A Thesis

Submitted to the Faculty of the Geology Department of Colby College in Fulfillment of the Requirements for Honors in Geology

Waterville, Maine

May 2012

GEODYNAMIC CONSTRAINTS ON THE FLOW OF SAMOAN-PLUME MANTLE INTO THE NORTHERN LAU BASIN

Except where reference is made to the work of others, the work described in this thesis is my own or was done in collaboration with my advisory committee.

Nathan Katsiaficas '12

Certificate of Approval:

Dr. Robert A. Gastaldo, Chair
Whipple-Coddington Professor
Department of Geology

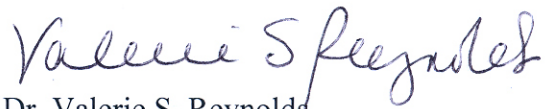

Dr. Valerie S. Reynolds
Clare Boothe Luce Assistant Professor
Department of Geology

Dr. Paul S. Hall
Assistant Professor
Department of Earth Sciences
Boston University

ABSTRACT

The northernmost portion of the Lau basin, South Pacific, features numerous geochemical and geophysical anomalies. These include: (1) a strong latitudinal gradient in the trace element and isotopic (Sr-Nd-Pb) enrichment of basalts erupted along the various back-arc spreading centers (BASCs) within the basin, (2) high $^{3}He/^{4}He$ (up to 28 times R_A, where R_A, the ratio in Earth's atmosphere, is 1.4×10^{-6}) in basalts erupted along some portions of the BASCs (e.g., Rochambeau Bank), and (3) the presence of trench-parallel shear-wave splitting near the Tonga arc. The occurrence of these anomalies has been attributed to the southward flow of mantle from the nearby Samoan hotspot into the northern Lau basin. Here, I present results from a series of numerical geodynamic experiments undertaken to test the viability of this hypothesis, and constrain both the total extent and the spatial distribution of any incursion of Samoan-plume mantle into the northern Lau basin. The experiments were conducted using the COMSOL Multiphysics Finite Element Modeling package to model mantle flow and melting within a 2-dimensional model domain corresponding to a north-south cross-section through the upper 400 km of the mantle, extending from the Pacific plate north of the Vitiaz lineament through the northern Lau basin. Experiments indicate that if the southward-flowing Samoan-plume mantle is hotter than ambient mantle, it would experience extensive melting due to adiabatic decompression as it moves from beneath the older (>100 Ma), colder, and thicker Pacific lithosphere to the younger (<5 Ma), warmer, and thinner lithosphere of the Lau basin south of the Vitiaz lineament. Experimental predictions of melt production are compared to bathymetric data from the northern Lau basin to constrain both the physical characteristics (e.g., temperature) and spatial distribution of the flow of Samoan-plume mantle into the basin.

ACKNOWLEDGEMENTS

There are so many people that played a role in making this honors thesis project a success. First, and foremost, I would like to thank Dr. Paul Hall for giving me this incredible research opportunity and for guidance over the summer (at Boston University) through the spring semester. I would also like to thank Dr. Robert A. Gastaldo and Dr. Valerie S. Reynolds for invaluable input and for keeping me relatively sane through the honors thesis process. I owe a huge debt of gratitude to Dr. Stephanie Taylor of the Colby Computer Science Department for coming to the rescue with substantial assistance related to data visualization in MATLAB. Many thanks as well to Dr. Matthew Jackson of Boston University and to his graduate student, Allison Price, for input and clarification of the helium isotopic data over the summer and during the fall semester. Additionally, I would like to thank Rohan Kundargi, graduate student at BU, for help over the summer and for letting me sleep on his couch during my senior Jan-Plan so that I could run the computer models at BU and obtain the results published in this thesis. I would also like to acknowledge Colby College Visiting Assistant Professor, Dr. Bruce Rueger, and classmates Gabriel Lerner and Brianna Lind (Colby College ’12), as well as Joshua Gray (Boston University ’13) for keeping me sane over the course of this project. Funding over the summer was provided by the Colby College Fund for Research and Internships in the Physical and Computational Sciences. Additional summer funding, and funding for travel to the 2011 Annual AGU meeting, was provided by NSF OCE-1061134 to Dr. Paul S. Hall. Funding for travel to 2011 Annual GSA meeting was provided by the Colby College Dean of Faculty and from the Colby College Geology Alumni Endowment.

TABLE OF CONTENTS

Page

INTRODUCTION

The Lau and North Fiji basins are located in a tectonically complex region (e.g., Zellmer and Taylor, 2001; Hart et al., 2004) in the South Pacific. These two back-arc basins are nestled between the Pacific and Indo-Australian plates, flanked by the Tonga trench to the east and the New Hebrides trench to the west (ancestral Vitiaz Trench, Fig. 1). The Tonga trench is the site of active westward subduction of the Pacific Plate beneath the Indo-Australian, Niuafo'ou, and Tongan plates, and experiences the fastest rates of convergence measured in the world, up to ~240 mm/yr (Bevis et al., 1995). To the north, the Vitiaz lineament separates the young (<5 Ma), thin lithosphere of the Lau and North Fiji basins from the old (>100 Ma), thick (relative to the Niuafo'ou plate) lithosphere of the Pacific plate (Brocher, 1985; Pelletier and Auzende, 1996).

The section of the Vitiaz lineament stretching east of 180 °W is suggested to have formed by the migration of the hinge of the subducting Pacific plate, tearing as the Tonga trench moved eastward towards the active region of the Samoan hotspot due to slab rollback (Hart et al., 2004). However, it also has been suggested that the full length of the Vitiaz lineament could be a "fossil" subduction zone, where subduction of the Pacific plate under the Australian plate occurred until ~12 Ma, at which time the Ontong-Java Plateau collided with the trench near the Solomon Islands (Brocher, 1985; Yan and Kroenke, 1993; Pelletier and Auzende, 1996; Pearce et al., 2007). Prior to the collision and resulting termination of active subduction, the Vitiaz trench was a continuous subduction zone from the Solomon Islands to Tonga. The present-day Vitiaz lineament acts essentially as an inactive transform boundary between the Australian plate and the Pacific plate.

The Samoan island chain, a volcanic island chain formed by the Samoan hotspot, lies just north of the Vitiaz lineament. The Samoan hotspot produces magmas with a distinct geochemical signature, characterized by elevated $^{3}He/^{4}He$ ratios (measuring up to 33.8 times R_A, where $R_A = 1.4 \times 10^{-6}$ [Farley et al. 1992; Graham, 2002; Jackson et al., 2007a]) relative to MORBs ($^{3}He/^{4}He = 8 \pm 1R_A$ [Class and Goldstein, 2005]), and high $^{87}Sr/^{86}Sr$ isotopic ratios (Fig. 2) (Jackson et al., 2007b). Although globally other hotspots produce magmas with a high $^{3}He/^{4}He$ isotopic signature (e.g., Hawaii, Galapagos, and Iceland), no other oceanic hotspot has a signature as isotopically enriched as the Samoan plume, with high $^{3}He/^{4}He$ in concert with low $^{143}Nd/^{144}Nd$ and high $^{87}Sr/^{86}Sr$ (Fig. 2) (Jackson et al., 2007b). Of particular interest, high $^{3}He/^{4}He$ is widely held to reflect the presence of either an undegassed, primordial lower mantle component (Lupton and Craig, 1975; Kurz et al., 1983; Hart et al., 1992; Farley et al. 1992) or an incompletely degassed mantle component in the source (Class and Goldstein, 2005).

The northernmost portion of the Lau basin features numerous geochemical and geophysical anomalies. These include: (1) a strong latitudinal gradient in trace element and isotopic (Sr-Nd-Pb) enrichment of basalts erupted along the various back-arc spreading centers (BASCs) within the basin (e.g., Volpe et al., 1988; Gill and Whelan, 1989; Poreda and Craig, 1992; Ewart et al., 1998; Turner and Hawkesworth, 1998; Pearce et al., 2007); (2) high $^{3}He/^{4}He$ (up to 28 R_A) in basalts erupted along some portions of the BASCs (e.g., Rochambeau Bank) (Sinton et al., 1985; Johnson et al., 1986; Johnson and Sinton, 1990; Sinton et al., 1993; Jackson et al., 2007a; Koppers et al., 2008; Jackson et al., 2010a,b) (Fig. 3); and (3) the presence of trench-parallel, shear-wave splitting near the Tonga arc, which is interpreted as indicating that the sub-arc mantle flows along the strike of the arc rather than

in the direction of subduction (Fig. 4; Smith et al., 2001). All of these anomalies have been attributed to the incursion of Samoan-plume mantle from the proximal Samoan hotspot through a "tear" (Turner and Hawkesworth, 1997) in the Pacific plate across the Vitiaz lineament, and into the shallow mantle of the Lau basin (Fig. 5) (Lupton and Craig, 1975; Giardini and Woodhouse, 1986; Volpe et al., 1988; Gill and Whelan, 1989; Poreda and Craig, 1992; Pearce et al., 1995; Turner and Hawkesworth, 1997; Ewart et al., 1998; Smith et al., 2001; Lupton et al., 2009). The Samoan plume signature—high $^{3}He/^{4}He$ and high $^{87}Sr/^{86}Sr$ isotopic ratios—is identifiably different from that of the upper mantle material within the northern Lau basin (low $^{3}He/^{4}He$ and low $^{87}Sr/^{86}Sr$) (e.g., Wright and White, 1987; Farley et al., 1992; Poreda and Craig, 1992; Workman et al., 2008; Kelley et al., 2006; Langmuir et al., 2006; Falloon et al., 2007; Jackson et al., 2007b; Escrig et al., 2009). In this study, I use numerical geodynamic experiments to test the viability of the hypothesized southward flow of Samoan-plume mantle and, in particular, to constrain the total extent and spatial distribution of any incursion of Samoan-plume mantle into the basin.

METHODS

Conceptual model

To evaluate the potential consequences of southward flow of Samoan-plume mantle across the Vitiaz lineament and into the Lau basin, mantle flow and melting are modeled for thermally buoyant mantle flowing along the base of the lithosphere across a step-change in thickness of the overlying lithosphere (Fig. 6). This abrupt change in thickness is founded upon the relationship between the age and thickness of the oceanic lithosphere as described by the half-space cooling (HSC) and plate (GDH1) (Stein and Stein; 1992) models, and

reflects the large difference in age between the Pacific and Niuafo'ou plates on either side of the Vitiaz lineament. The HSC model predicts temperature (T) as a function of age and depth by,

$$T(z,t) = T_m \operatorname{erf}\left(\frac{z}{2\sqrt{\kappa t}}\right) \quad (1)$$

where z is depth in m, t is the age of the lithosphere in seconds, T_m is the temperature at the ridge axis (°C), and κ is thermal diffusivity ($m^2\ s^{-1}$). In Equation # 1, erf denotes the error function. The GDH1 plate model assumes a constant plate thickness, L (km), and approximates temperature (T) by,

$$T = T_m \left[\frac{z}{L} + \sum_{n=1}^{\infty} \frac{2}{n\pi} \sin\left(\frac{n\pi z}{L}\right) \exp\left(-\frac{n^2\pi^2\kappa t}{L^2}\right)\right] \quad (2)$$

where T_m is not only the temperature at the ridge axis, as in the HSC model (Eq. # 1), but is also the temperature at the base of the plate. Parameters z, κ, and t are the same as in Equation # 1. Temperature is approximated in Equation # 2 for a summation of 4 (n = 4). Solving for temperature in the HSC and GDH1 models allows for the creation of temperature profiles over depth. Temperature profiles for two plates, 5 Myr and 100 Myr in age, are plotted in Figure 7A for both models based on Equations # 1-2 with the constant parameter values set as defined in Table 1. This study makes use of a temperature-dependent, diffusion-creep rheology that ignores the dependence on pressure, grain size, and water content (e.g., van Keken et al., 2008) (see Eq. # 6 below) to solve for the dynamic viscosity (η_{diff}) (i.e., Eq. # 6 solves for η_{diff} as a function of T). Figure 7B displays viscosity contours for the two plates with ages of 5 and 100 Myr generated from Equation # 6 using the predicted temperatures in Figure 7A for the HSC and GDH1 plate models. Just as the temperature defines viscosity, viscosity defines lithospheric thickness. To determine a

theoretical plate thickness for the HSC and GDH1 models, this study uses a viscosity value of 10^{22} Pascal seconds, Pa s—approximately one order of magnitude above the average upper mantle viscosity, ~10^{21} Pa s (Mitrovica, 1996)—to mark the base of the plate. High viscosities (> 10^{22} Pascal seconds, Pa s) denote lithosphere, whereas low viscosities (< 10^{22} Pa s) denote asthenosphere. In Figure 7B, the effective lithospheric thickness from the HSC and GDH1 models for both plates is the vertical distance from the surface down to the base of the plate, or the depth at which the viscosity curve reaches 10^{22} Pa s. The models use lithospheric age (*t*) to solve for temperature (Eqs. # 1-2), which is then used to solve for viscosity (Eq. # 6), ultimately yielding an effective plate thickness. Therefore, the differences between the contours of temperature and viscosity, and different effective lithospheric thicknesses in Figure 7 between the two plates are purely a function of age.

For lithosphere younger than 20 Myr, both HSC and GDH1 models predict similar plate thicknesses. This is evident in Figure 7, in which the predicted profiles of temperature and viscosity for the 5 Myr-old plate are approximately identical for the two models. However, for a plate that is older than 20 Myr, the predicted temperature profiles begin to diverge. In such a scenario, the HSC model predicts a thicker cold thermal boundary layer and, hence, a greater effective plate thickness, than does the GDH1 model. And, eventually, it predicts temperature and viscosity profiles that are more steeply sloped (Fig. 7) for oceanic lithosphere older than 60-70 Myr (i.e., the 100 Myr-old plate). Despite these differences, both models predict that the thermal boundary layer and, thus, the plate itself, increase in thickness with age. In the northern Lau basin, the positive correlation between age and the thickness of the thermal boundary (i.e., effective lithospheric thickness) sets up a situation where, moving across the Vitiaz lineament, there is a sudden decrease in the thickness of the

overlying plate, proportional to the vast age difference between the Pacific and Niuafo'ou plates (Fig. 6).

Numerical geodynamic model

Although the northern Lau basin and the surrounding region are tectonically complex (e.g., Zellmer and Taylor, 2001; Hart et al., 2004), and despite the fact that regional mantle flow is likely 3-dimensional (3-D) (e.g., Smith et al., 2001; Kincaid and Griffiths, 2003), the north-south-trending, latitudinal gradients of isotopic depletion indicate that the flow responsible for producing the melt depletion is primarily 2-dimensional (2-D). Therefore, a simplified, 2-D geometry is considered to be suitable for a first attempt at modeling mantle flow at this location. Flow and melting are modeled using the COMSOL Multiphysics finite element package, assuming an idealized, 2-D geometry, corresponding to a vertical cross-section through the upper 400 km of mantle oriented perpendicularly to a discontinuity in lithospheric age (Fig. 8). A depth of 400 km is used because there is an increase in viscosity that occurs just below this depth in the upper mantle, and because 400 km lies below where melting occurs in the model and prevents boundary effects from influencing it.

The model domain is discretized with a free triangular mesh of 6,715 triangular elements, and spans 1600 km in the horizontal. Figure 8 depicts the model domain for the reference conditions. Thermally buoyant mantle is introduced to the system through a plume conduit with a radius (r_p) of 50 km positioned at the bottom-left corner of the model. Under reference conditions, the distance between the start of the plume (the left boundary of the domain) and the transform boundary is 400 km; the step-change in thickness between the two plates occurs at 400 km (Fig. 8).

Within this 2-D domain, mantle flow is modeled as the flow of a viscous, Boussinesq fluid with an infinite Prandtl number (ratio of a fluid's kinematic viscosity to its thermal diffusivity [Fowler, 2005]). Velocity within the mantle is derived from equations for the conservation of mass and momentum for a viscous fluid with an infinite Prandtl number,

$$\nabla \cdot u = 0 \tag{3}$$

$$\nabla \cdot \tau - \nabla p = \rho g_i \tag{4}$$

where u is velocity, p is dynamic pressure, and τ is the deviatoric stress tensor. Deviatoric stress is related to velocity by

$$\tau = 2\eta\dot{\epsilon} = \eta(\nabla u + (\nabla u)^T) \tag{5}$$

where η is the effective dynamic viscosity and $\dot{\epsilon}$ is the strain rate tensor. This study makes use of a simplified, temperature-dependent, diffusion-creep rheology that ignores dependence on pressure, grain size, and water content (e.g., van Keken et al., 2008),

$$\eta_{diff}(T) = A_{diff}\exp\left(\frac{E_{diff}}{RT}\right). \tag{6}$$

The effective viscosity, η, is derived from the minimum of η_{diff} and a maximum viscosity, η_{max}, which is utilized for computational efficiency.

Temperature (T) inside the model domain is acquired from the equation for the conservation of energy for a medium with constant density (ρ), heat capacity (C_p), and thermal conductivity (k), including a source term to account for latent heat related to melting (Φ_L),

$$\frac{\partial T}{\partial t} = -\rho C_p(u \cdot \nabla)T + \nabla \cdot (k\nabla T) - \Phi_L \tag{7}$$

A comprehensive list of values for all variables and parameters appears in Table 1.

Boundary conditions for the model domain are set to govern temperature and velocity at the four boundaries. Velocity conditions are set to no slip ($u = 0$; $v = 0$) at the top boundary, and free slip ($u = 0$; $dv/dy = 0$) at the left boundary. The right and bottom boundaries are both stress free ($du/dx = 0$; $dv/dy = 0$), but normal flow conditions ($u = 0$) also are imposed at the bottom. This allows for flow to encounter no resistance when moving orthogonal to the bottom boundary, while material can flow out of the domain along the right boundary. Potential temperatures are set to T_0 (T_0 = 0 °C) at the top boundary and T_m (1350 °C [Fowler, 2005]) at the bottom boundary. The left and right boundaries are set to insulating temperature conditions ($\partial T/\partial x = 0$). In the bottom left-hand corner of the domain, the plume is generated by setting temperatures to the ambient temperature in the mantle (T_m) plus an additional excess plume temperature, ΔT_p. Under the initial reference conditions, ΔT_p is set to 150 °C. These boundary conditions are included with the initial model configuration in Figure 8 for the reference condition.

Initially, the left plate (Fig. 8) has an age (t_0p_1) set to 100 Myr, and for 7 of the 10 experiments, the right plate has an age (t_0p_2) of essentially 0 Myr. The younger plate is set to 0 Myr because with the long, 20 Myr duration of the model, melting and flow would be diminished quickly by the effects of lithospheric cooling. The ages in the experiment are close to those of the Pacific and Niuafo'ou plates (>100 Myr and <5 Myr).

To calculate the amount of melting within the model domain, a Lagrangian particle method (e.g., Hall and Kincaid, 2003; Kincaid and Hall, 2003) is utilized, in which particles are injected into the domain and tracked at each time-step during the duration of the model. The model simulates flow for a period of 20 million years, with 201 time-steps at intervals of 100,000 years, starting at time "0." In all, the positions of 100,000 particles are tracked over

time based on their positions at the previous time-step. At each time-step, the change in composition for each particle is interpolated to model melting and depletion. In each experiment, melting is calculated using a Lagrangian particle method based on Hall and Kincaid (2003). Melting and depletion are gleaned from two parameters being solved for in the experiments, instantaneous melt (*dF*) and depletion (*Fx*). With the onset of the plume, *dF* increases for nearly all numerical experiments due to materials being displaced into lower pressures and succumbing to decompression melting; however, after the first several hundred thousand years, melting activity equilibrates with the conditions in the domain. *Fx* is at its highest at the upper boundary of the model domain, reflecting high depletion within the oceanic plates due to their origination from partial melting of MORB upper-mantle. The *dF* and *Fx* parameters, viewed alongside the temperature and time parameters, depict interesting scenarios for each of the numerical experiments.

RESULTS

A series of 10 numerical experiments was undertaken to model mantle flow and melting associated with a plume crossing a step-like discontinuity in lithospheric structure. The computational numerical experiments model the evolution of plume-material flow across a discontinuity in lithospheric age and thickness over a period of 20 Myr. To best characterize mantle flow, melting, and depletion of mantle material across a step-wise change in lithospheric thickness, numerical experiments were undertaken to consider the effects of three important parameters. The effects of plume-excess temperature (ΔT_p), the distance between the plume and the transform boundary (Δx_p), and the age of the younger plate ($t_0 p_2$) are investigated, with each of these experimental parameters varied systematically, one at a

time. A range of values was considered for each parameter; a complete explanation of the experimental parameter values for each of the ten experiments is found in Table 2.

The first of the ten experiments (Exp. 1, Table 2) is the reference scenario. Under these conditions: plume-excess temperature, ΔT_P, is 150 °C; the distance between the plume and the transform boundary, Δx_p, is set to 400 km; and the age of the younger plate, $t_0 p_2$, is set to 0 Myr. Over the course of the run duration, the plume moves through the model domain, across the transform boundary, towards the opposite end of the domain. The integrated melt generation is plotted vs. x-position in the domain (m) (Fig. 9) for three times in the duration that depict conditions before the plume has reached the transform boundary, just as the plume has reached it, and after the plume has passed the boundary. The highest peaks of integrated *dF* occur before the plume has reached the transform boundary (1.9 Myr). At the time of encountering the boundary (3.9 Myr), the peak integrated instantaneous melting has decreased, and melting activity is not as widespread as it was at 1.9 Myr. By 9.9 Myr, melting activity has decreased further and is confined spatially to a small range of positions, clustered around 600 km (200 km past the plate boundary). Figure 10B features three snapshots of the model for the reference scenario, depicting the plume's progress through the domain with instantaneous melting (*dF)* contoured on top of the temperature field, corresponding to the same three steps shown in in Figure 9B. The instantaneous melting contours in Figure 10B agree with the relationship between *dF* and x-position in Figure 9B, indicating that the most active and widespread melting occurs before the plume has reached the transform. However, melting only occurs in the younger plate, beyond the transform. Melting at this stage of plume evolution in the model is caused by the displacement of mantle material ahead of the plume to shallower depths, where it undergoes

decompression melting due to lower pressures. By the time the plume has reached the transform, it is no longer pushing as much mantle material up ahead of it, and the spatial range over which high melting activity is occurring has decreased. When the plume has moved beyond the transform boundary, melting activity only occurs over a small area (Fig. 9B). The melting trend over the model duration for the reference conditions is a decrease in the lateral extent of melting.

Plume potential temperature

Over the course of four computational numerical experiments (Exps. 1-4; Table 2), the plume-excess temperature (ΔT_p) is varied systematically to understand the model's sensitivity to this parameter. Plume-excess temperatures of 100, 150, 200, and 250 °C are considered. For numerical experiments varying ΔT_p at temperatures at or below 150 °C (Exps. 1-2; Table 2), instantaneous melting (*dF*) is more widespread and remains widespread longer in the model with higher temperatures but, ultimately, melting becomes less widespread over time and areas of higher melting activity become confined to the region just beyond the transform boundary at 400 km (Figs. 9-11). At ΔT_p = 100°C, melting does not continue through the 20-Myr duration and may terminate earlier (Figs. 9A and 10A). For numerical experiments with ΔT_p at temperatures from 200 – 250 °C (Exps. 3-4, Table 2), the highest melting activity occurs after the mantle plume has traveled past the transform boundary and continued beneath the younger plate (Figs. 12-13), reaching further away from the plume (Fig. 14). For all experiments varying ΔT_p, the highest melting (max *dF*) hovers around a region ~600 km away from the plume (200 km past the transform boundary) (Fig. 15). Higher plume-excess temperatures allow melting to persist longer and lead to greater depletion of mantle material. However, the controlling factor on melting seems to be time, as

it relates to lithospheric thickness per the half-space cooling (HSC) model. The thermal boundary layers of the plates, and, specifically, the younger plate in the domain, become thicker during the course of the numerical experiments and eventually prevent decompression melting from occurring. Higher plume-excess temperatures allow the plume to move faster and cross the transform sooner, leading to prolonged melting and lessening the effects of half-space cooling.

Plume – transform distance

As with the preceding suite of numerical experiments, a set of four numerical experiments (Exps. 1, 5-7; Table 2) were conducted to evaluate the effect of the distance between the plume and the transform boundary (Δx_p). Distances of 200, 400, 600, and 800 km were examined for their impact on melting and depletion. Varying the distance between the plume and the transform, as might be imagined, has a marked impact on melting and depletion. For a transform boundary as far as 400 km away from the plume, melting persists through the entire experiment (Figs. 16-18). Melting activity dies out more quickly (Figs. 19-21) with increasing distances of 600 or 800 km. Again, melting is confined to a small area, ~200 km past the plate margin, even though the transform boundary shifts position in each of these experiments. Melting activity steadily decreases in magnitude and duration with increasing Δx_p, and eventually ceases to persist through the full 20-Myr period in the experiments with Δx_p values of 600 and 800 km (Exps. 6-7) (Fig. 22). While the cessation of melting activity may be affected slightly by temperature diffusion out of the plume as it travels through the domain, the factor with the most influence on melting is, once again, time (per HSC model). Higher Δx_p values cause the plume to take longer to reach the transform boundary. With time, the thermal boundary of the younger plate thickens until the plate is so

old that, by the time the plume reaches the transform and crosses to the younger plate, decompression melting cannot occur.

Age of younger plate

The age of the younger plate (t_0p_2), was varied in a final suite of numerical experiments (Exps. 1, 8-10; Table 2). The experiments were run for initial plate ages of 0, 25, 50, and 75 Myr. There were no occurrences of melting or depletion in experiments varying t_0p_2 except for the reference experiment (Exp. 1, Table 2), in which Δx_p was set to 0 Myr. The thermal boundary of the younger plate becomes so thick with increasing age that, even for an initial age of 25 Myr, melting via adiabatic decompression is unable to take place. Altogether, the four numerical experiments indicate that the age of the overlying plate has a profound effect on melting by limiting the depths to which underlying mantle material can ascend.

DISCUSSION

All three of the experimental parameters tested in this study, plume-excess temperature (ΔT_p), distance between the plume and the transform boundary (Δx_p), and the age of the younger plate (t_0p_2), have major effects on melting in the model. Varying ΔT_p or Δx_p drastically changes the time necessary for the plume to reach the transform boundary. A higher plume-excess temperature, or shorter distance between the plume and plate boundary, decreases the time it takes for the plume to reach the boundary. With less time, per the HSC model, the plume encounters a thinner thermal boundary layer and more melting occurs. The opposite is true for a lower plume-excess temperature or larger distance between the plume and the plate boundary. For both parameters, melt generation begins in the domain at the

same distance past the plate margin, at ~ 20 km. However, the maximum distance from the transform boundary at which melt generation occurs (excluding melting artifacts at 800 km in all experiments, see Fig. 8 caption) increases with higher ΔT_p or lower Δx_p. This means that, with high plume-excess temperatures or shorter distances between the plume and the transform boundary, melting occurs further away in the younger plate. Varying t_0p_2 has the greatest impact on melting of all the parameters, because instead of affecting how fast the plume is going to move, or how far it has to travel before crossing the boundary, it changes the thickness of the thermal boundary layer of the younger plate from the very start of the model duration. As a result, adiabatic decompression melting is immediately stifled and mantle material is unable to rise from depth to lower pressures where melting can occur. Unless t_0p_2 is very low, melting does not occur, and there is no melting activity in the younger plate or anywhere in the domain.

These results indicate that decompression melting occurs for a range of plume-excess temperatures and with a relatively short distance between a plume, beneath an older plate, and a transform boundary separating the older plate from a much younger one. Sleep (2002) predicts that decompression melting should occur for situations where a plume flows across a lithospheric discontinuity separating two plates with a difference in age, at a transform plate boundary. He finds little evidence to support this phenomenon, examining several hotspots including Réunion, Discovery, and St. Helena. At these hotspots, Sleep (2002) notes the absence of significant volcanism associated with plume-material crossing the transform plate boundaries and declares a lack of real-life examples where plume material is in a position to cross over large-age-offsets at transform boundaries. Sleep (2002), therefore, suggests that perhaps the differences in lithospheric thicknesses at transform boundaries between two

plates of different ages are less pronounced than might be expected. Sleep (2002) assumes that a plume will flow across a transform boundary between two plates with an age difference and undergo decompression melting, but fails to consider half-space cooling and the age of the younger plate. However, the results from this present study where the age of the younger plate is varied demonstrate that even with an age difference of 75 Myr (Exp. 8, Table 2) between the two plates, melting may not occur. Instead, it is the age of the younger plate, not the difference between its age and the older plate, that is important. Melting is directly related to the thickness and, thus, the age of a plate. Results from this study suggest that if the younger plate is young enough (i.e. ~<5 Myr), melting may occur. There may be very few examples in which a mantle plume is in close proximity to a transform that separates the overlying plate from a very young plate. However, there is at least one instance of such a scenario, one that Sleep (2002) failed to notice, in the northern Lau basin.

In the South Pacific, the Vitiaz lineament separates the >100 Myr-old Pacific plate, to the north, from the <5 Myr-old Niuafo'ou plate, to the south. Samoan plume-mantle from the hotspot located 400 km to the north of the lineament is hypothesized to flow across the lineament and into the northern Lau basin. The distance between the plume and the Vitiaz lineament combined with the ages of the two plates limits the relevant experiments in this study to Experiments 1-4. These experiments vary plume-excess temperature from 100-250 °C. In all cases, melting occurs just beyond the transform boundary, in the younger plate. But, with increasing ΔT_p, melting persists further away from the transform boundary. For ΔT_p = 100 or 150 °C, the highest melting, and resulting volcanic activity, would be expected to occur soon after crossing the plate boundary, extending as far as ~200 km away. At temperatures of 200 and 250 °C, high melt generation is nearly ubiquitous after the transform

on the younger plate. While the very highest melting remains in the region just beyond the transform, volcanic activity should be evident up to and perhaps beyond ~400 km (for ΔT_p = 200 °C) and ~600 km (for ΔT_p = 250 °C) south of the transform boundary.

In the northern Lau basin, volcanic activity is expressed as topographic highs, or excess bathymetry. By comparing the predicted volcanic activity for the scenarios depicted in Experiments 1-4 to the bathymetry south of the Vitiaz lineament (Fig. 23), ΔT_p may be constrained. In Figure 23, just south of the Vitiaz lineament, is a small region of high seafloor elevation that corresponds to two seamounts between ~178 °W and 175 °W. These seamounts are not in close proximity to any known hotspots and there are no other regions of seafloor elevation of comparable magnitude to the east or west. Model results from this study suggest that this region of elevated bathymetry as the most likely corridor, or zone of entry along the lineament, through which Samoan-plume mantle is entering (Fig. 23). This pathway is the "tear" described by Millen and Hamburger (1998) and Grovers and Wortel (2005), whereby buoyant plume material from the Samoan hotspot crosses the Vitiaz lineament into the northern Lau basin. This interpretation is supported by the north-south gradients in Sr, Nd, and Pb isotopes (Nohara et al., 1994; Auzende et al., 1995; Pearce et al., 2007; Regelous et al., 2008). Regions of high $^3He/^4He$ isotopic ratios associated with Samoan-plume mantle (Fig. 3) are consistent with the zone from 178 °W – 175 °W, marking the narrow window through which Samoan-plume mantle enters the Lau basin.

If ΔT_p were 200 °C or 250 °C, too much melt would be produced over too widespread of a distance. Depletion would be widespread as well, yielding a swath of lower R_A values for $^3He/^4He$ isotopic ratios south of this point. However, this is not the case. The seamounts are located on the northern tip of Rochambeau Rifts, which is the region in the Lau basin

with the highest $^{3}He/^{4}He$ ratios (Figs. 3, 23). The region of excess bathymetry in Figure 23 extends to 30 ', or ~56 km at most, suggesting that Experiments 1-2, with plume-excess temperatures of 100 and 150 °C, are the best analogues to this region. If ΔT_p were less than 100 °C, it is doubtful that the observed seamounts would have formed. But, if temperature was much greater than 150 °C, too much melting might occur, and the observed highest R_A values for $^{3}He/^{4}He$ would probably not be distributed in a tight cluster by Rochambeau Bank.

CONCLUSION

This study has presented results from a series of 2-D numerical experiments designed to test the viability of, and constrain the total extent and spatial distribution of, the incursion of Samoan-plume mantle into the northern Lau basin. I find that for a plume in close proximity to a transform boundary separating it from a younger plate, the occurrence of melting hinges on the age of the younger plate. As the plume flows across the transform boundary, adiabatic decompression melting may occur if the younger plate is <5 Myr in age. The temperature of the plume and the distance between it and the boundary are important factors that affect how long it takes the plume to reach the transform boundary, and, in turn, how thick the thermal boundary layer beneath the younger plate is upon the plume's arrival. The thickness of the thermal boundary layer is the critical parameter governing whether or not decompression melting can occur, by controlling the depth to which material may rise.

Two seamounts within a region of elevated bathymetry between 178 °W and 175 °W, north of Rochambeau Rifts, mark the most probable location along the Vitiaz lineament for incursion of Samoan-plume mantle and are consistent with the trend in high $^{3}He/^{4}He$ isotopic ratios in the northern part of the basin. Here, I estimate a plume-excess temperature of 100-

150 °C from the seafloor topography and the spatial trend in enriched helium signatures. Future work related to this study includes tests for the sensitivity of the model to different amounts of particles than the 100,000 used in these experiments. Additionally, forward-modeling of trace-and-major element composition could provide useful corroborating evidence for the model. Research related to measuring $^{3}He/^{4}He$ isotopic ratios of the two seamounts north of Rochambeau Rifts, and high-resolution, swath bathymetry, is to be completed in the near future, and will help to further constrain the conduit through which Samoan-plume mantle flowed into the Lau basin.

REFERENCES CITED

Auzende, J.M., M. Pelletier, and J.P. Eissen (1995). The North Fiji Basin: Geology Structure and Geodynamic Evolution, in *Backarc Basins: Tectonics and Magmatism*, B. Taylor, ed., Plenum Press, New York, pp. 139-175.

Bevis, M., F.W. Taylor, B.E. Schutz, J. Recy, B.L. Isacks, S. Helu, R. Singh, E. Kendrick, J. Stowell, B. Taylor, and S. Calmant (1995). Geodetic observations of very rapid convergence and back-arc extension at Tonga arc. *Nature*, **374**, 249-251.

Brocher, T.M. (1985). On the age progression of the seamounts west of the Samoan islands, S.W. Pacific, in *Investigations of the Northern Melanesian Borderland, Circum-Pacific Council for Energy and Mineral Resources Earth Science Series*, T.M. Brocher, ed., **3**, pp. 173-185.

Class, C., and S.L. Goldstein (2005). Evolution of helium isotopes in the Earth's mantle. *Nature*, **436**, 1107-1112.

Dickinson, W.R. (2006). Temper Sands in Prehistoric Oceanian Pottery: Geotectonics, Sedimentology, Petrography, Provenance. *Geological Society of America Special Papers*, **406**, 1-160.

Escrig, S., A. Bézos, S.L. Goldstein, C.H. Langmuir, and P.J. Michael (2009). Mantle source variations beneath the Eastern Lau Spreading Center and the nature of subduction components in the Lau basin-Tonga arc system: *Geochem. Geophys. Geosyst.* (G-cubed), **10**, doi: 10.1029/2003GC000542.

Ewart, A., K.D. Collerson, M. Regelous, J.I. Wendt, and T. Niu (1998). Geochemical evolution within the Tonga-Kermadec Lau arc back-arc systems: The role of varying mantle wedge composition in space and time. *J. Petrol.*, **39**, 331-368.

Falloon, T.J., L.V. Danyushevsky, T.J. Crawford, R. Maas, J.D. Woodhead, S.M. Eggins, S.H. Bloomer, D.J. Wright, S.K. Zlobin, and A.R. Stacey (2007). Multiple mantle plume components involved in the petrogenesis of subduction-related lavas from the northern termination of the Tonga arc and northern Lau basin: Evidence from the geochemistry of arc and backarc submarine volcanics. *Geochem. Geophys. Geosyst.* (G-cubed), **8**, doi:10.1029/2007GC001619.

Farley, K.A., J.H. Natland, and H. Craig (1992). Binary mixing of enriched undegassed (primitive?) mantle components (He, Sr, Nd, Pb) in Samoan lavas. *Earth Planet. Sci. Lett.*, **111**, 183-199.

Fowler, C.M.R. (2005). *The Solid Earth: An Introduction to Global Geophysics*, 2nd ed., 685 pp., Cambridge Univ. Press, Cambridge.

Giardini, D., and J.H. Woodhouse (1986). Horizontal shear flow in the mantle beneath the Tonga arc. *Nature*, **319**, 551-555.

Gill, J., and P. Whelan (1989). Early rifting of an oceanic island arc (Fiji) produced shoshonitic to tholeiitic basalts. *J. Geophys. Res.*, **94**, 4561-4578.

Graham, D.W. (2002). Novle Gases in Geochemistry and Cosmochemistry, in *Reviews in Mineralogy and Geochemistry*, D. Porcelli, C.D. Ballantine, and R. Weiler eds., Mineralogy Society of America, pp. 247-317.

Grovers, R., and M.J.R. Wortel (2005). Lithosphere tearing at STEPS faults: Response to edges of subduction zones. *Earth Planet. Sci. Lett.*, **236**, 505-523.

Hall, P.S. and C. Kincaid (2003), Melting, dehydration and the dynamics of off-axis plume-ridge interaction. *Geochem.Geophys.Geosyst.*, **4** (8510).

Hall, P.S., L.B. Cooper, and T. Plank (2012). Thermochemical evolution of the sub-arc mantle due to back-arc spreading. *J. Geophys. Res.*, **117**, doi:10.1029/2011JB008507.

Hart, S.R., E.H. Hauri, L.A. Oschmann, and J.A. Whitehead (1992). Mantle plumes and entrainment: isotopic evidence. *Science*, **256**, 517-520.

Hart, S.R., M. Coetzee, R.K. Workman, J. Blusztajn, K.T.M. Johnson, J.M. Sinton, B. Steinberger, and J.W. Hawkins (2004). Genesis of the Western Samoa seamount province: age, geochemical fingerprint and tectonics. *Earth Planet. Sci. Lett.*, **24**, 427-439.

Hilton, D.R., K. Hammerschmidt, G. Loock, and H. Priedrichsen (1993). Helium and argon isotope systematics of the central Lau Basin and Valu Fa Ridge: Evidence of crust/mantle interactinos in a back-arc basin. *Geoch. Cosmochim. Acta*, **57**, 2819-2841.

Hirth, G., and D.L. Kohlstedt (2003). Rheology of the upper mantle and the mantle wedge: A view from the experimentalists, in *Inside the Subduction Factory: Geophysical Monograph*, **138**, J. Eiler, ed., American Geophysical Union, pp. 83-105.

Honda, M., D.B. Patterson, I. McDougall, and T.J. Falloon (1993). Noble gases in submarine pillow basalt glasses from the Lau Basin: Detection of a solar component in backarc basin basalts. *Earth Planet. Sci. Lett.*, **120**, 135-148.

Jackson, M.G., S.R. Hart, A.A.P. Koppers, H. Staudigel, J. Konter, J. Blusztajn, M.D. Kurz and J.A. Russell (2007a). Evidence for the return of subducted continental crust in Samoan lavas. *Nature*, **448**, 684-697.

Jackson, M.G., M.D. Kurz, S.R. Hart, and R.K. Workman (2007b). New Samoan lavas from Ofu Island reveal a hemispherically heterogeneous high $^{3}He/^{4}He$ mantle. *Earth Planet. Sci. Lett.*, **128**, 183-197.

Jackson, M.G., M.D. Kurz, and S.R. Hart (2009a). Helium and neon isotopes in phenocrysts from Samoan lavas: Evidence for heterogeneity in the terrestrial $^{3}He/^{4}He$ mantle. *Earth Planet. Sci. Lett.*, **287**, 519-528.

Jackson, M.G., S.R. Hart, N. Shimizu, and J. Blusztajn (2009b). Pervasive cpx-whole rock isotopic disequilibrium in Polynesian hotspot lavas: Evidence supporting isotopic variability in olivine and clinopyroxene-hosted melt inclusions. *Geochem. Geophys. Geosyst.* (G-cubed), **10**, doi:10.1029/2008GC002324.

Jackson, M.G., R. Carlson, M.D. Kurz, P.D. Kempton, D. Francis, and J. Blusztajn (2010a). Evidence for the survival of the oldest terrestrial mantle reservoir. *Nature*, **466**, 853-856.

Jackson, M.G., S.R. Hart, J.G. Konter, A.A.P. Koppers, H. Staudigel, M.D. Kurz, J. Blusztajn, and J.M. Sinton (2010b). The Samoan hotspot track on a "hotspot highway": Implications for mantle plumes and a deep Samoan mantle source. *Geochem. Geophys. Geosyst.* (G-cubed), **11**, doi:10.1029/2010GC003232.

Johnson, K.T.M., and J.M. Sinton (1990). Petrology, tectonic setting, and the formation of back-arc basin basalts in the North Fiji Basin. *Geol. Jahrb., Reihe D*, **92,** 517-545.

Johnson, K.T.M., J.M. Sinton, and R.C. Price (1986). Petrology of seamounts northwest of Samoa and their relation to Samoan volcanism. *Bull. of Volcanol.*, **48**, 225-235.

Kelley, K.A., T. Plank, T.L. Grove, E.M. Stolper, S. Newman, and E. Hauri (2006). Mantle melting as a function of water content beneath back-arc basins. *J. Geophys. Res.*, **113**, doi:10.1029/2002GC000433.

Kincaid, C., and R.W. Griffiths (2003). Laboratory models of the thermal evolution of the mantle during rollback subduction. *Nature*, **425**, 58-62.

Kincaid, C. and P.S. Hall (2003), Role of back arc spreading in circulation and melting at subduction zones, *J. Geophys. Res.*, **108**, doi:10.1029/2001JB001174.

Koppers, A.P., J.A. Russel, M.G. Jackson, J.G. Konter, H. Staudigel, and S.R. Hart (2008). Samoa reinstated as a primary hotspot trail. *Geology*, **36**, 435-438.

Langmuir, C.H., A. Bezos, S. Escrig, and S.W. Parman (2006). Chemical systematics and hydrous melting of the mantle in back-arc basins, in *Back-Arc Spreading systems: Geological, Biological, Chemical, and Physical Interactions, Geophys. Monogr. Ser.*, **166**, D.M. Christie et al., eds., American Geophysical Union, pp. 87-146.

Lupton, J.E., and H. Craig (1975). Excess ^{3}He in oceanic basalts, evidence for terrestrial primordial helium. *Earth Planet. Sci. Lett.*, **26**, 133-139.

Lupton, J.E., R.J. Arculus, R.R. Greene, L.J. Evans, and C.I. Goddard (2009). Helium isotope variations in seafloor basalts from the Northwest Lau Backarc Basin: Mapping the influence of the Samoan hotspot. *Geophys. Res. Lett.*, **36**, doi:10.1029/2009GL039468.

Millen, D.W., and M.W. Hamburger (1998). Seismological evidence for tearing of the Pacific plate at the northern termination of the Tonga subduction zone. *Geology*, **26**, 659-662.

Mitrovica, J.X. (1996). Haskell [1935] revisited. *J. Geophys. Res.*, **101**, doi:10.1029/95JB03208.

Nohara, M., K. Hirose, J.P. Eissen, T. Urabe, and M. Joshima (1994). The North Fiji Basin basalts and their magma sources: Part II. Sr-Nd isotopic and trace element constraints. *Mar. Geol.*, **116**, 179-195.

Pearce, J.A., M. Ernewein, S.H Bloomer, L.M. Parson, B.J. Murton, and L.E. Johnson (1995). Geochemistry of Lau Basin volcanic rocks: Influence of ridge segmentation and arc proximity, in *Volcanism associated with extension at consuming plate margins: Geological Society London Special Publications*, J.L. Smellie, ed., **81**, pp. 53-76.

Pearce, J.A., P.D. Kempton, and J.B. Gill (2007). Hf-Nd evidence for the origin and distribution of mantle domains in the SW Pacific. *Earth Planet. Sci. Lett.*, **260**, 98-114.

Pelletier, B., and J.M. Auzende (1996). Geometry and structure of the Vitiaz Trench Lineament (SW Pacific). *Mar. Geophy. Researches*, **18**, 305-335.

Poreda, R.J., and H. Craig (1992). He and Sr isotopes in the Lau Basin mantle: depleted and primitive mantle components. *Earth Planet. Sci. Lett.*, **113**, 487-493.

Regelous, M., S. Turner, T.J. Falloon, P. Taylor, J. Gamble, and T. Green (2008). Mantle dynamics and mantle melting beneath Niuafo'ou Island and the northern Lau back arc basin. *Cont. Min. Pet.*, **156**, 103-118.

Sinton, J.M., K.T.M. Johnson, and R.C. Price (1985). Petrology and geochemistry of volcanic rocks from the Northern Melanesian Borderland, in *Investigations of the Northern Melanesian Borderland, Circum-Pacific Council for Energy and Mineral Resources Earth Science Series,* T.M. Brocher, ed., **3**, pp. 35-65.

Sinton, J.M., R.C. Price, K.T.M. Johnson, H. Staudigel, and A. Zindler (1993). Petrology and geochemistry of submarine lavas from the Lau and North Fiji back-arc basins, in *Basin Formation, Ridge Crest Processes, and Metallogenesis in the North Fiji Basin*, *Circum-Pacific Council for Energy and Mineral Resources Earth Science Series*, L.W. Kroenke and J.V. Eade, eds., **15**, pp. 119-135.

Sleep, N.H. (2002). Local lithospheric relief associated with fracture zones and ponded plume material. . *Geochem. Geophys. Geosyst.* (G-cubed), **3**, doi:10.1029/2002GC000376.

Smith, G.P., D.A. Wiens, K.M. Fischer, L.M. Dorman, S.C. Webb, and J.A. Hildebrand (2001). A complex pattern of mantle flow in the Lau Backarc. *Science*, **292**, 713-716.

Stein, C.A., and S. Stein (1992). A model for the global variation in oceanic depth and heat flow with lithospheric age. *Nature*, **359**, 123-129.

Turner, S., and C. Hawkesworth (1997). Constraints on flux rates and mantle dynamics beneath island arcs from Tonga-Kermadec lava geochemistry. *Nature*, **389**, 568-573.

Turner, S.P., and C.J. Hawkesworth (1998). Using geochemistry to map mantle flow beneath the Lau basin. *Geology*, **26**, 1019-1022.

van Keken, P.E., C. Currie, S.D. King, M.D. Behn, A. Cagnioncle, J. He, R. F. Katz, S.-C. Lin, E. M. Parmentier, M. Spiegelman, and K. Wang (2008), A community benchmark for subduction zone modeling, *Phys. Earth Planet. Int.*, **171**, 187-197.

Volpe, A.M., J.D. MacDougall, and J.W. Hawkins (1988). Lau Basin basalts (LBB): trace element and Sr-Nd isotopic evidence for heterogeneity in backarc basin mantle. *Earth Planet. Sci. Lett.*, **90**, 174-186.

Wright, E., and W.M. White (1987). The origin of Samoa: New evidence from Sr, Nd, and Pb isotopes. *Earth Planet. Sci. Lett.*, **81**, 151-162.

Workman, R.K., S.R. Hart, M.G. Jackson, M. Regelous, K. Farley, J. Blusztajn, M. Kurz, and H. Staudigel (2004). Recycled metasomatized lithosphere as the origin of the enriched mantle II (EM2) end-member: Evidence from the Samoan Volcanic Chain. *Geochem. Geophys. Geosyst.* (G-cubed), **5**, doi: 10.1029/2003GC000623.

Workman, R.K., J.M. Eiler, S.R. Hart, and M.G. Jackson (2008). Oxygen isotopes in Samoan lavas: Confirmation of continent recycling. *Geology*, **36**, 551-554.

Yan, C.Y., and L.W. Kroenke (1993). A plate tectonic reconstruction of the Southwest Pacific, 0-100 Ma, in *Proceedings of the Ocean Drilling Program. Scientific Results*, W.H. Berger et al., eds., **130**, pp. 697-709.

Zellmer, K.E., and B. Taylor (2001). A three-plate kinematic model for Lau Basin opening, *Geochem. Geophys. Geosyst.* (G-cubed), **2**, doi:2000GC000106.

Table 1. List of parameters along with their reference value or dimensions as used in the computational, numerical experiments.

Parameter	Symbol	Value	Dimensions
Constants			
Activation energy	E_{diff}	335	kJ mol^{-1}
Adiabatic gradient	ΔT_{adb}	0.3	°C km^{-1}
Age, older plate	$t_0 p_1$	100	Myr
Density	ρ	4000	kg m^{-3}
Dynamic viscosity, maximum	η_{max}	1 x 10^{26}	Pa s
Gas constant	R	8.314472	J $°C^{-1}$ mol^{-1}
Gravitational acceleration	g_i	10	m s^{-2}
Heat capacity	C_p	1250	J $°C^{-1}$ mol^{-1}
Kinematic viscosity	η_k	1 x 10^{18}	m^2 s^{-1}
Mantle water content[a]	C_{H_2O}	0.1	wt%
Potential temperature, mantle[b]	T_m	1350	°C
Potential temperature, surface	T_0	0	°C
Pre-exponential constant	A_{diff}	1.32043 x 10^9	Pa s
Thermal conductivity	K	5.000	W m^{-1} $°C^{-1}$
Thermal expansivity	α_0	2.5 x 10^{-5}	$°C^{-1}$
Geometric Parameters			
Plume conduit radius	r_p	50000	m
Experimental Parameters			
Plume-excess temperature	ΔT_p	100, 150, 200, 250	°C
Age, younger plate	$t_0 p_2$	0.01, 25, 50, 75	Myr
Distance, plume-transform boundary	Δx_p	200, 400, 600, 800	km
Variables			
Depth	z	-	m
Depletion	Fx	-	-
Deviatoric stress	τ	-	Pa
Dynamic pressure	p	-	Pa
Dynamic viscosity, diffusion creep	η_{diff}	-	Pa s
Dynamic viscosity, effective	η	-	Pa s
Instantaneous melt	dF	-	-
Latent heat loss	Φ_L	-	°C s^{-1}
Temperature	T	-	°C
Strain rate	$\dot{\epsilon}$	-	s^{-1}
Time	t	-	Myr
Velocity	u	-	m s^{-1}

a: (Hall et al., 2012)

b: (Fowler, 2005)

Table 2. Description of numerical experiments with associated experimental parameters.

Experiment No.	Plume-excess temperature (°C)	Plume-transform distance (km)	Age of younger plate (Myr)
Reference			
1	150	400	0
Plume-excess temperature (ΔT_p)			
2	100	400	0
3	200	400	0
4	250	400	0
Initial distance, plume-transform (Δx_p)			
5	150	200	0
6	150	600	0
7	150	800	0
Age of younger plate ($t_0 p_2$)			
8	150	400	25
9	150	400	50
10	150	400	75

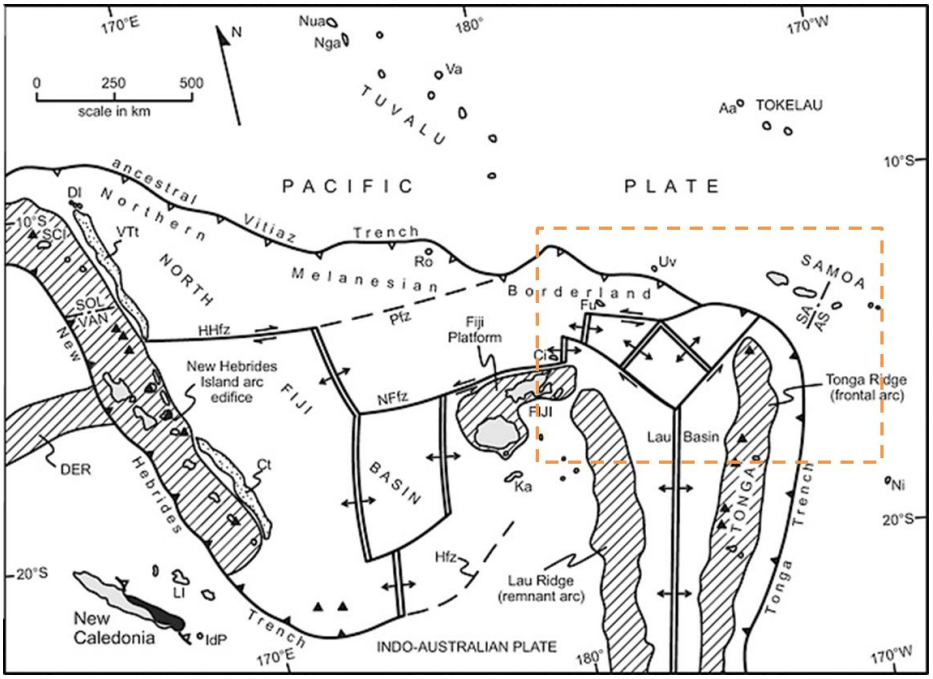

Figure 1. Map of the study area and surrounding region in the Southern Pacific Ocean depicting the complex tectonic setting of the Lau and North Fiji basins. The area within the dashed lines corresponds to the mapped region in Figure 3 (after Dickinson, 2006).

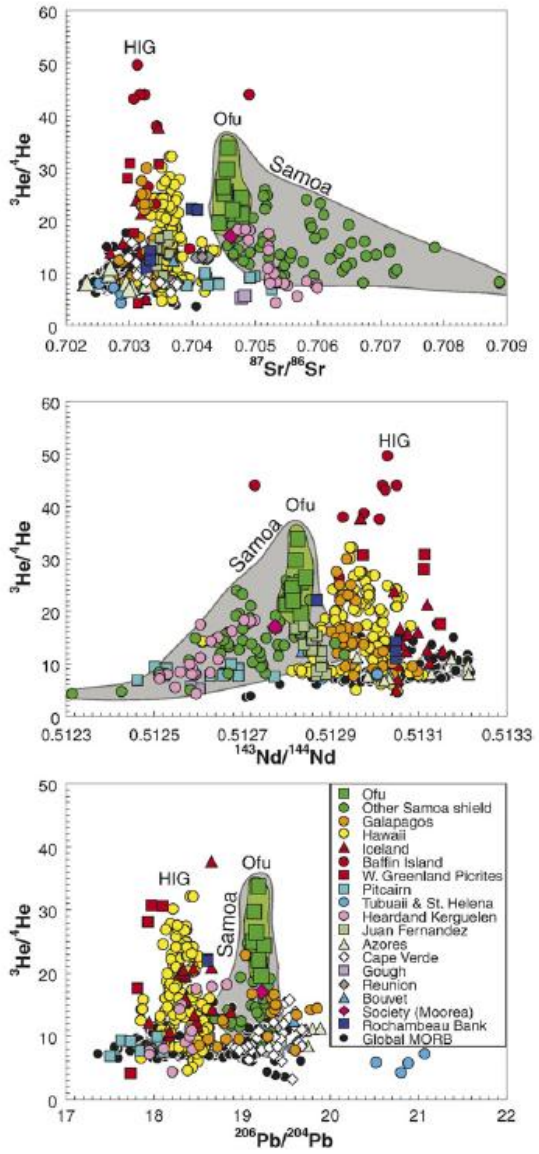

Figure 2. Isotopic data for global MORB and selected global hotspots. The highest $^{3}He/^{4}He$ ratios occur in the HIG (Hawaii, Iceland, and Galapagos) rocks.. However, Samoan lavas exhibit more of an enriched signature, with lower $^{143}Nd/^{144}Nd$ and higher $^{87}Sr/^{86}Sr$, and higher $^{206}Pb/^{204}Pb$ than the HIG lavas. MORB isotopic ratios (black circles) are markedly lower in $^{3}He/^{4}He$ than Samoan lavas. (Figure from Jackson et al., 2007b).

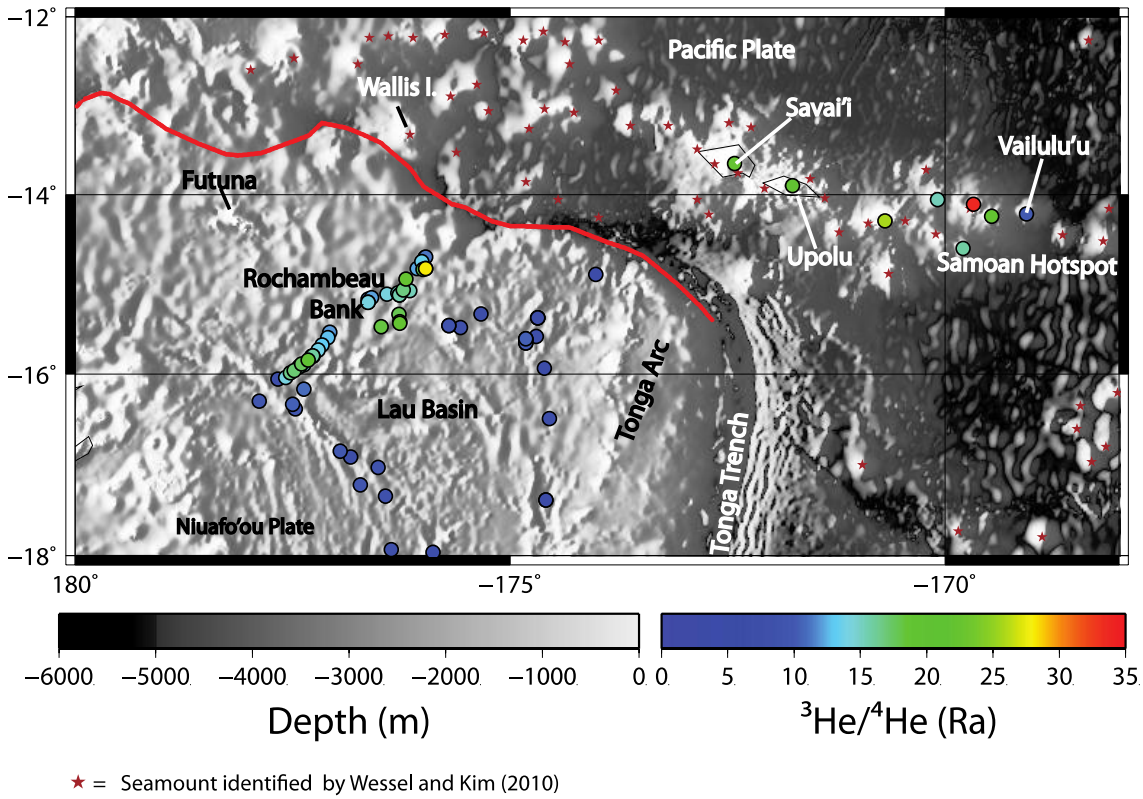

Figure 3. Map of the northern Lau basin in the Southern Pacific Ocean, showing the location of helium isotope measurements (colored circles) where colors indicate $^{3}He/^{4}He$ ratios, ranging from 0 (dark blue) to 35 (red) R_A (ratio to atmosphere). Data from Poreda and Craig (1992), Hilton et al. (1993), Honda et al. (1993), Jackson et al. (2007a,b; 2009a,b), and Lupton et al. (2009).

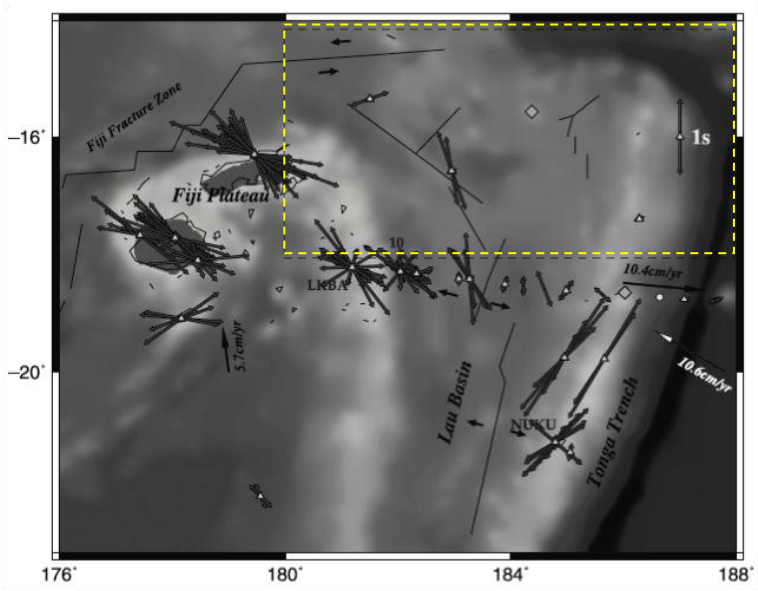

Figure 4. Map of the Lau and North Fiji basins showing shear-wave splitting in the region, (after Smith et al. 2001). The orientation of the vectors indicates the azimuth of the fast splitting direction, while the length of the vectors corresponds to the magnitude of the observed splitting. The direction of splitting changes from trench-parallel in the east edge of the map, near the Tonga Trench, to trench-perpendicular in the west, in the back-arc and beneath Fiji. Assuming anisotropy due to lattice preferred orientation of olivine crystals, splitting direction is considered to indicate direction of mantle flow. The dashed line corresponds to the mapped area in Figure 3.

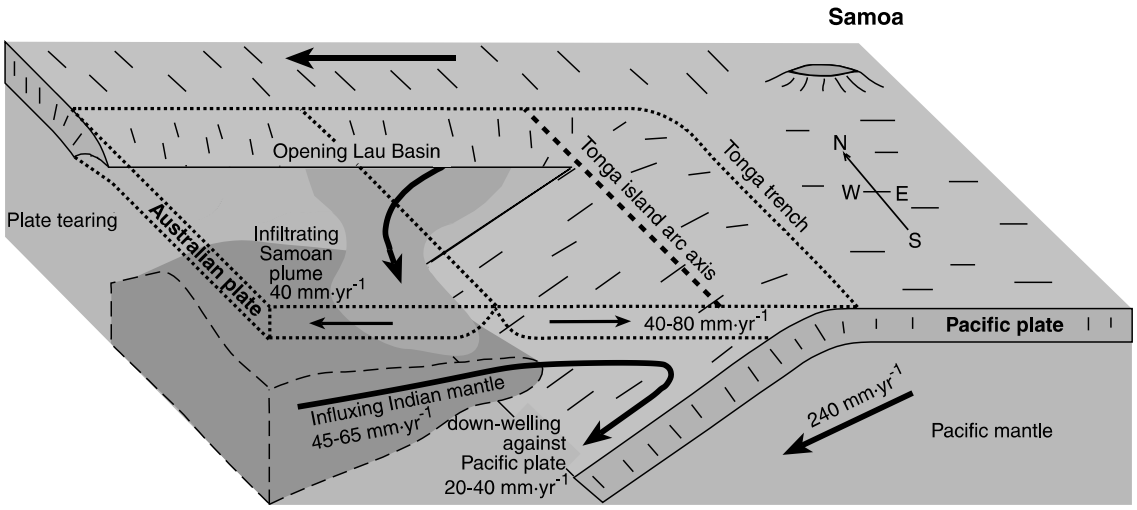

Figure 5. The distribution of geochemical anomalies, along with the observed trench-parallel, shear-wave splitting (see Fig. 4), are interpreted to indicate movement of material from the Samoan mantle plume southward, leaking through a tear in the subducting Pacific plate along the Vitiaz lineament, into the northern Lau Basin (from Smith et al., 2001).

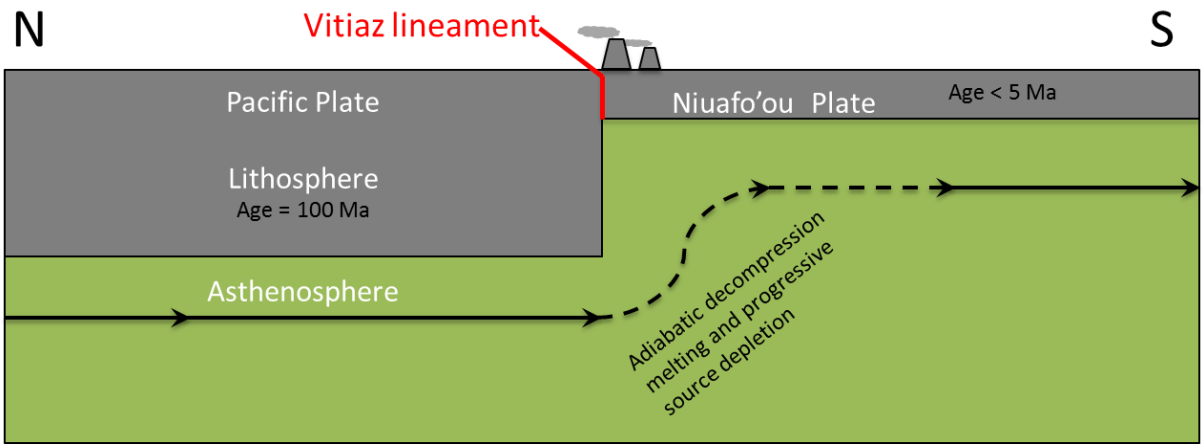

Figure 6. Conceptual model of north-south flow across a step-like change in lithospheric thickness. Decompression leads to melting (dashed arrow), resulting in volcanism near the discontinuity in lithospheric age and progressive depletion of residual mantle material.

A. B.

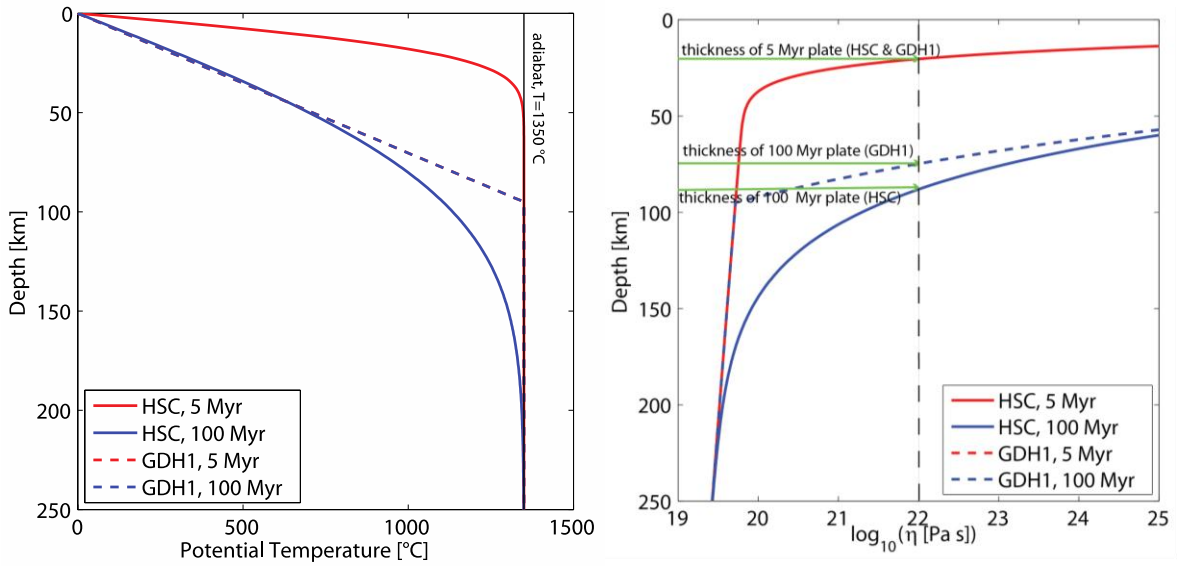

Figure 7. Variations in plate thickness across the Vitiaz lineament. The Pacific plate, north of the Vitiaz lineament, is older than the Niuafo'ou plate to the south (>100 Myr vs. < 5 Myr). The result is a significant change in lithospheric thickness across the lineament. **A**. Temperature profiles for oceanic lithosphere with ages of 5 Myr and 100 Myr are shown, using a half-space cooling model (HSC) and the global depth-and-heat (GDH1) plate model of Stein and Stein (1992). **B**. Illustration of the corresponding viscosity profiles assuming a simple diffusion-creep law and a dry olivine rheology (e.g., Hirth and Kohlstedt, 2003). In both the HSC and the GDH1 models, the older lithosphere results in a thicker thermal boundary layer and, hence, a thicker plate. When results from both models are compared, the HSC model predicts a thicker plate and a steeper temperature profile for older plates (i.e., the 100 Myr plate).

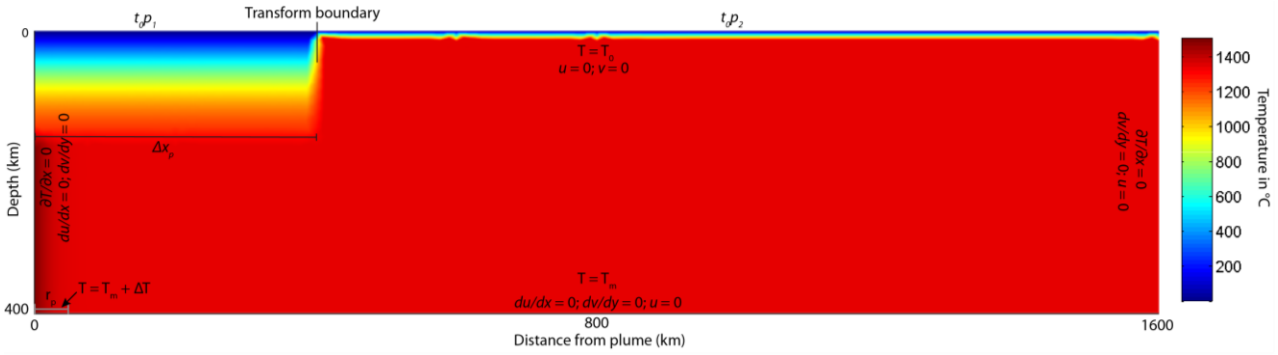

Figure 8. Initial and boundary conditions for the numerical geodynamic model. Colors indicate the initial distribution of potential temperatures within the model domain (range: 0 °C – 1500 °C). Temperature and velocity within the model domain are obtained by solving the equations of conservation (mass, momentum, heat) for a viscous, Boussinesq fluid with an infinite Prandtl number using the COMSOL Multiphysics Finite Element modeling package, subject to the indicated boundary conditions. For the subsequent figures displaying melting in relation to position in the model domain, there are artificial points for melt generation at 800 km caused by the boundary conditions on the right of the model, which allow for the flow of materials out of the domain.

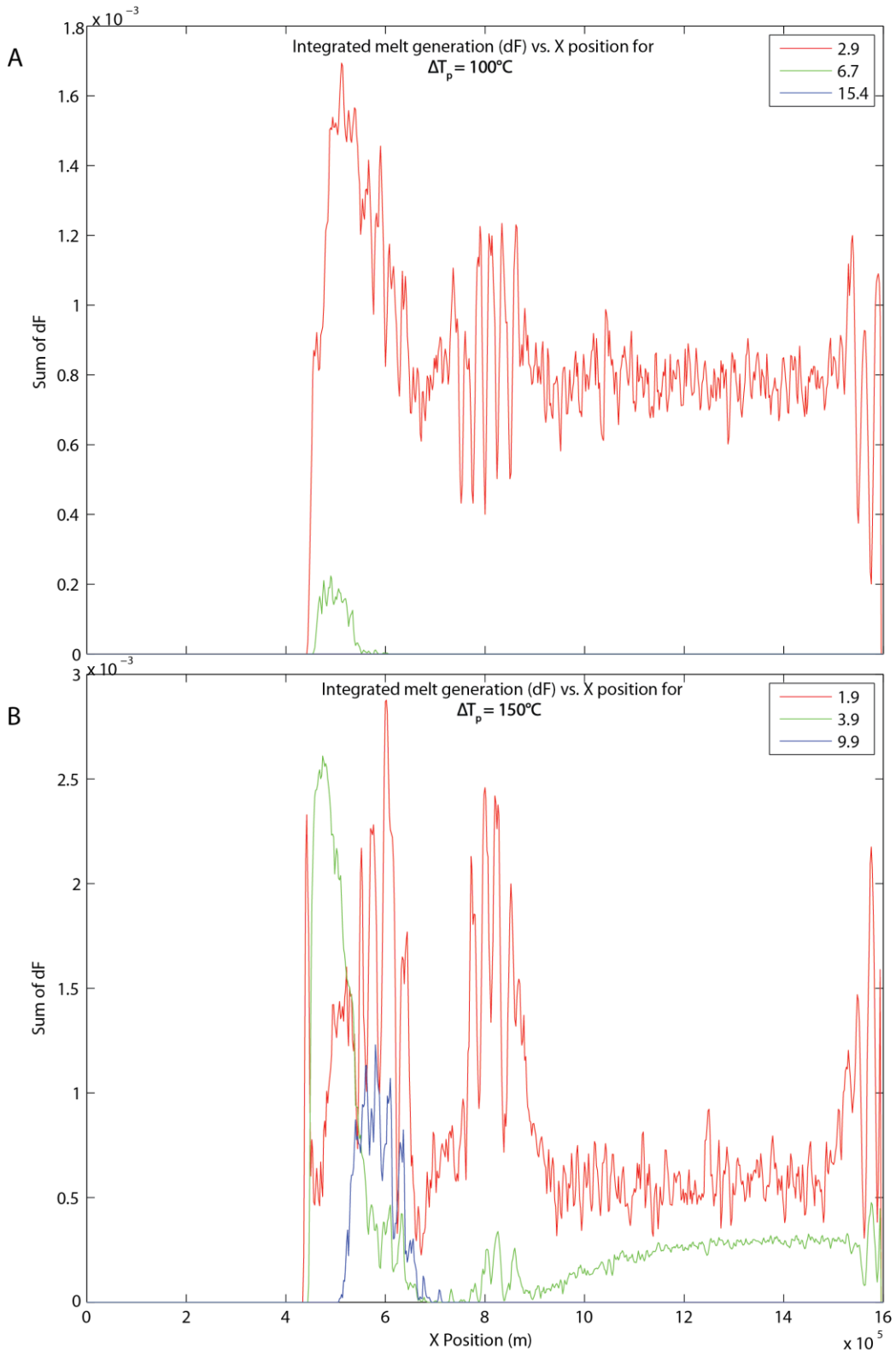
A
x 10^-3
Integrated melt generation (dF) vs. X position for
ΔT_p = 100°C
2.9
6.7
15.4
Sum of dF
B
x 10^-3
Integrated melt generation (dF) vs. X position for
ΔT_p = 150°C
1.9
3.9
9.9
Sum of dF
X Position (m)
x 10^5

Figure 9

Figure 9. Melt generation (*dF*) integrated over depth and plotted against x-position (m) within the modeling domain for Experiments 1-2, which have differing plume-excess temperatures (ΔTp). The sum, or integral of *dF*, is plotted for three times in the course of the model corresponding to significant events in the progress of the plume, and depicts conditions: (1) before the plume has reached the plate boundary, (2) at the "moment" or time-step when the plume arrives at and crosses the boundary, and (3) after the plume has crossed the boundary and continued onward. **A.** Integrated *dF* for a plume-excess temperature of 100 °C at 2.9, 6.7, and 15.4 Myr. There is no line plotted for *dF* after the plume has crossed the transform because there is no longer melt generation for a ΔT_p of 100 °C. Of the times depicted, the most melting occurs prior to the plume's arrival at the boundary, decreasing by a factor of nearly 9 by the time it reaches and crosses the boundary. The peak melt generation at both times occurs just beyond the transform. **B.** Integrated *dF* for reference conditions, with a ΔT_p of 150 °C at 1.9, 3.9, and 9.9 Myr. Melt generation prior to impacting of the boundary is high, marked by several peaks on the graph, as the plume pushes material lying beyond the plate boundary up to shallower depths and adiabatic decompression melting takes place. By 3.9 Myr, when the plume has reached the transform, melting is focused primarily in the region just beyond the boundary and is less widespread than earlier. Six million years later, at 9.9 Myr, the plume has progressed beyond the transform, and melt generation has decreased and shifted further away from the plate boundary.

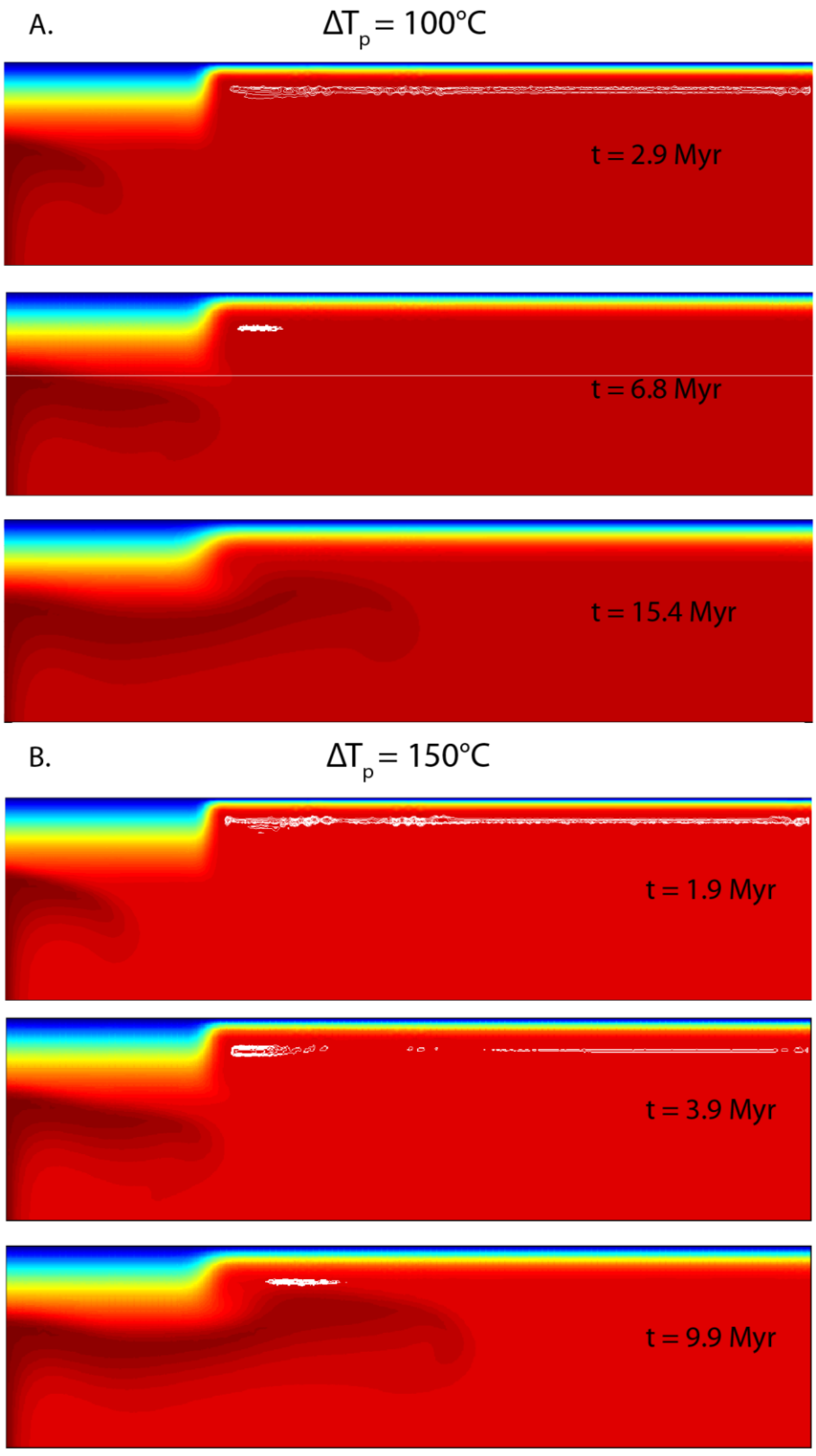
A.
$\Delta T_p = 100°C$
t = 2.9 Myr
t = 6.8 Myr
t = 15.4 Myr
B.
$\Delta T_p = 150°C$
t = 1.9 Myr
t = 3.9 Myr
t = 9.9 Myr

Figure 10

Figure 10. Snapshots of the model domain at ΔT_p of **A**) 100 °C and **B**) 150 °C, corresponding to the times and plots in Figures 9A and 9B, respectively. The colors reflect temperature within the domain, with the exception of the white contours, which represent instantaneous melting, or *dF* for the specific time-step.

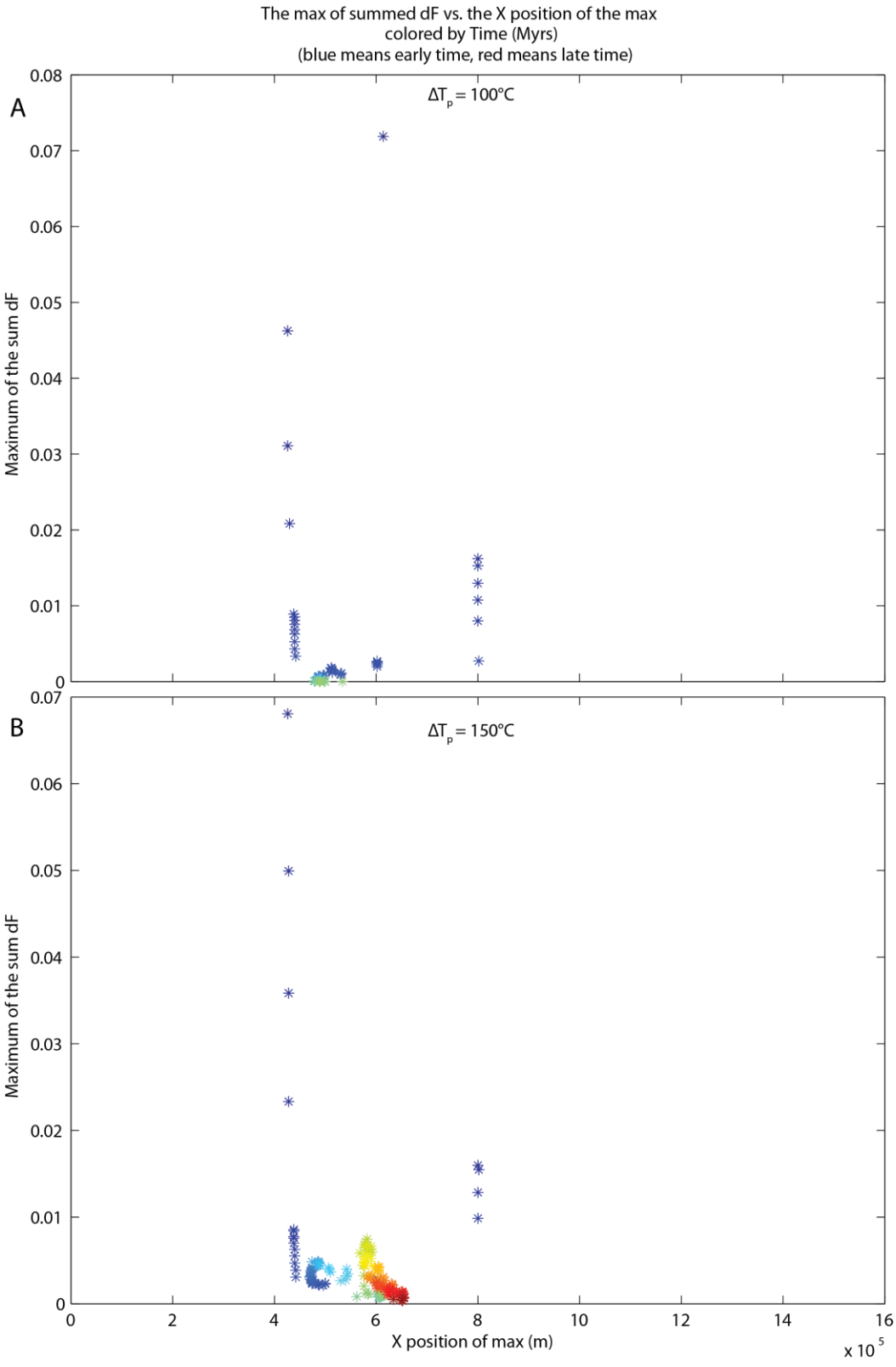
The max of summed dF vs. the X position of the max
colored by Time (Myrs)
(blue means early time, red means late time)
A
ΔT_p = 100°C
B
ΔT_p = 150°C
Maximum of the sum dF
X position of max (m)
x 10^5
0
0.01
0.02
0.03
0.04
0.05
0.06
0.07
0.08
2
4
6
8
10
12
14
16

Figure 11

Figure 11. Maximum integrated instantaneous melting (*dF*) vs. x-position within the model domain (m) for Experiments 1-2. Colors reflect time in Myr, ranging from 0 Myr (blue), to 20 Myr (red). **A.** Depiction of Experiment 2, with ΔT_p = 100 °C. As shown in Figures 9A and 10A, melting in Experiment 2 does not persist for the full period of 20 Myr—shown here by the absence of colors corresponding to the latter ~9-10 Myr. **B.** Plot for Experiment 1 for ΔT_p = 150 °C. Similar to Figures 9B and 10B, maximum melting activity migrates from ~450-550 km early-on, to ~600-650 km at the end of the model run. The 50 °C change between **A** and **B** increases the amount and duration of melting, and seems to also increase the spatial extent over which melting occurs.

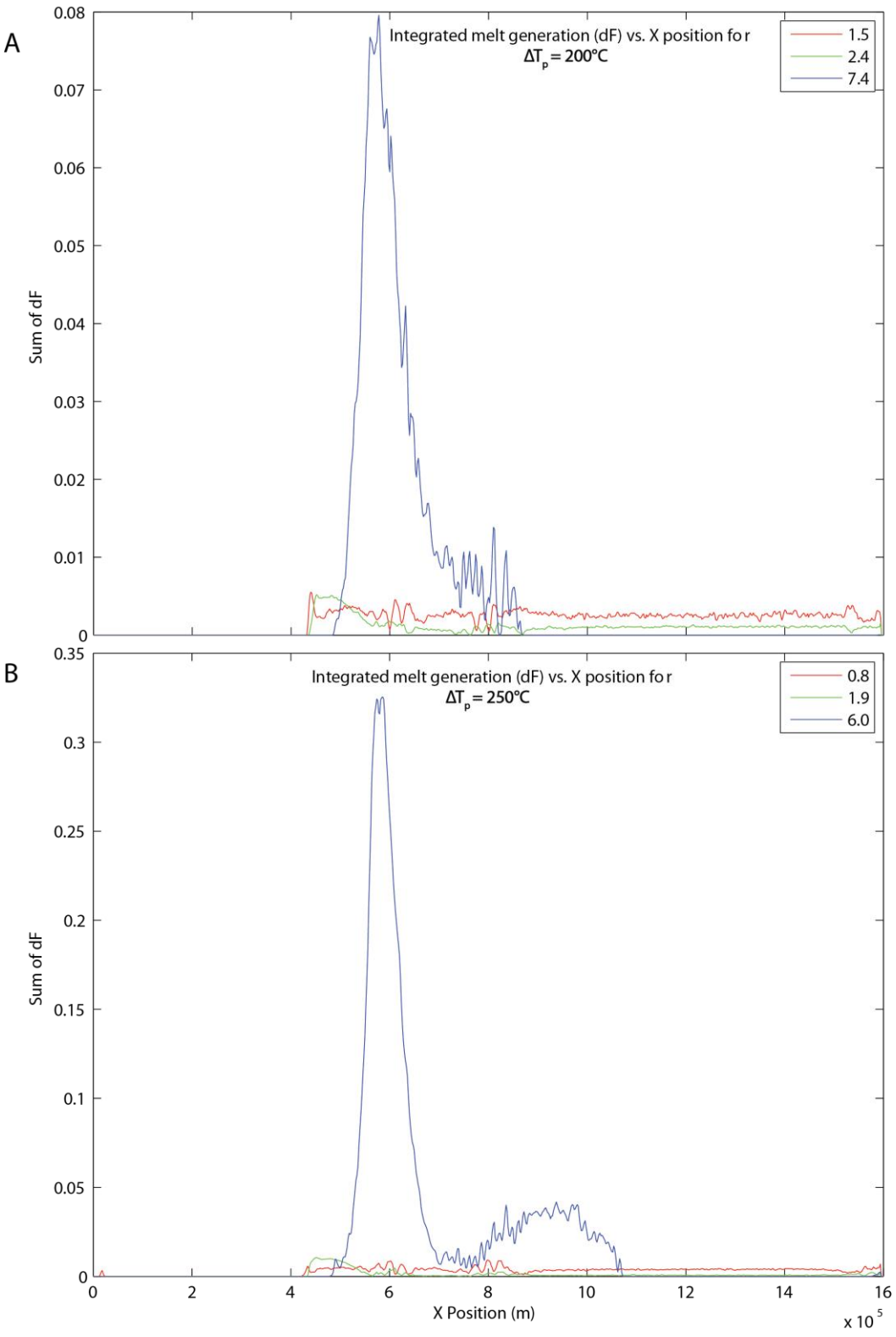
A
Integrated melt generation (dF) vs. X position for
ΔTp = 200°C
1.5
2.4
7.4
Sum of dF
0.08
0.07
0.06
0.05
0.04
0.03
0.02
0.01
0
B
Integrated melt generation (dF) vs. X position for
ΔTp = 250°C
0.8
1.9
6.0
Sum of dF
0.35
0.3
0.25
0.2
0.15
0.1
0.05
0
0
2
4
6
8
10
12
14
16
X Position (m)
x 10^5

Figure 12

Figure 12. Integrated *dF* for Experiments 3-4 (Table 2), with ΔT_p values of 200 °C and 250 °C. **A.** For a plume with ΔT_p = 200 °C, the highest melt generation does not occur before the plume reaches the transform (1.5 Myr), nor even upon its arrival at the plate boundary (2.4 Myr). But, instead, the highest generation of melt occurs well afterwards (7.4 Myr) when the plume has continued moving further away. **B.** A plume with ΔT_p = 250 °C exhibits the same trend except that it has higher melt generation than does **A**, with almost identically shaped curves of integrated melt generation at all three times plotted (0.9, 1.8, and 6 Myr). Melt generation increases with time in both **A** and **B**, even after the plume reaches the transform plate boundary and continues to progress further away.

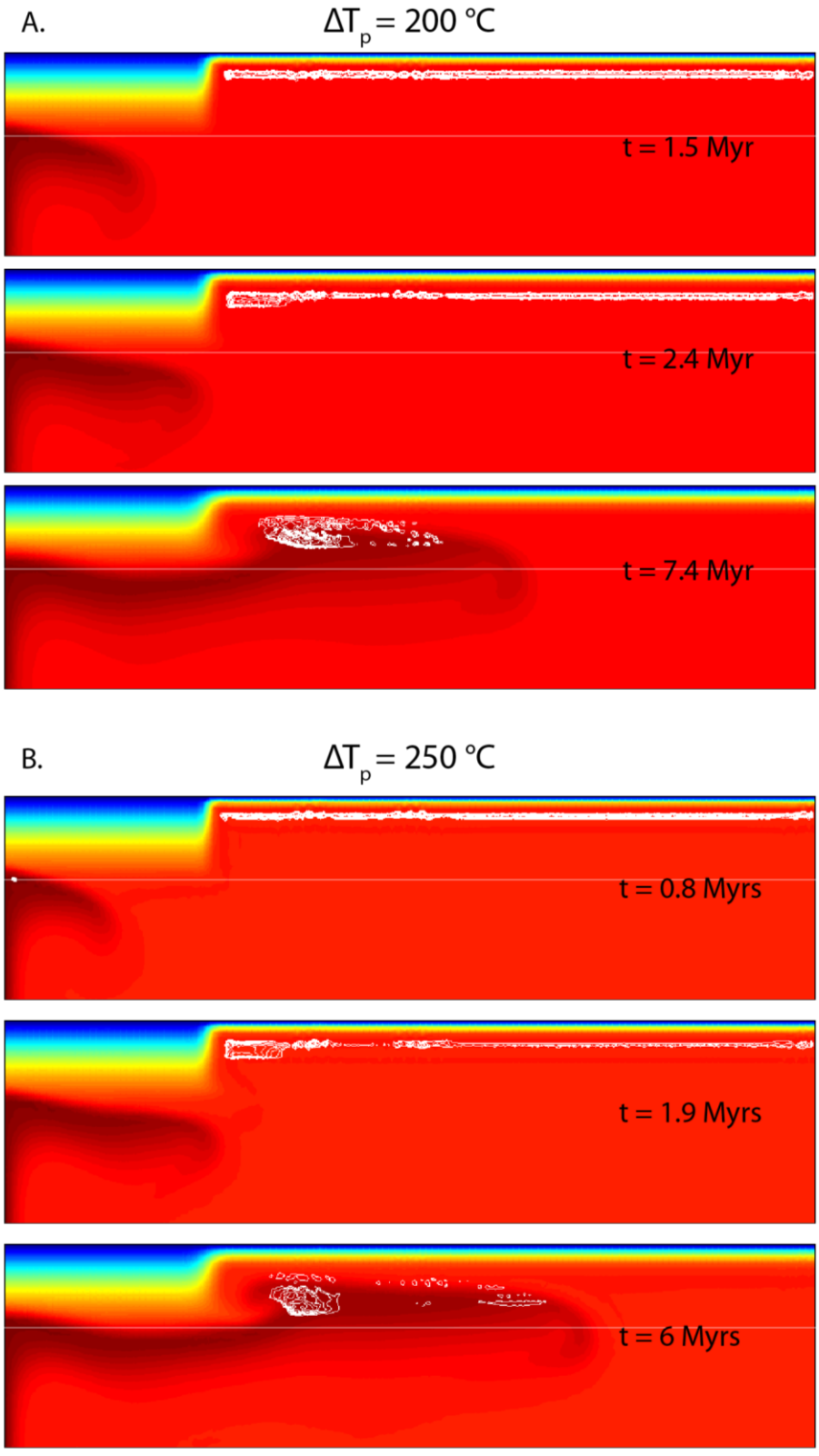
A.
ΔT_p = 200 °C
t = 1.5 Myr
t = 2.4 Myr
t = 7.4 Myr
B.
ΔT_p = 250 °C
t = 0.8 Myrs
t = 1.9 Myrs
t = 6 Myrs

Figure 13

Figure 13. Snapshots of the model domain corresponding to the times in Figure 12. The colors reflect temperature within the domain (see Fig. 8), with the exception of the white contours, which denote instantaneous melt generation (*dF*) for the specific time-step. **A.** Depiction of the model domain for ΔT_p = 200 °C corresponding to the graph in Figure 12A. **B.** Corresponds to Figure 12B, displaying the model domain for ΔT_p = 250 °C. In **A** and **B**, the increase in the amount and extent of integrated melt generation over time is attributed to the higher ΔT_p values, which diminish the effect of time on the thickness of the thermal boundary layer (i.e., per HSC). This allows melting to continue to occur even after the plume has crossed the transform boundary. In addition to affecting melt quantity, the high ΔT_p values also cause waves to propagate after the plume has moved beyond the discontinuity at 400 km, originating from a spot at ~600 km in the domain and continuing to the far-right boundary. The waves are most abundant for ΔT_p = 250 °C (Exp. 4) because they begin to occur earlier than they do for ΔT_p = 200 °C (Exp. 3).

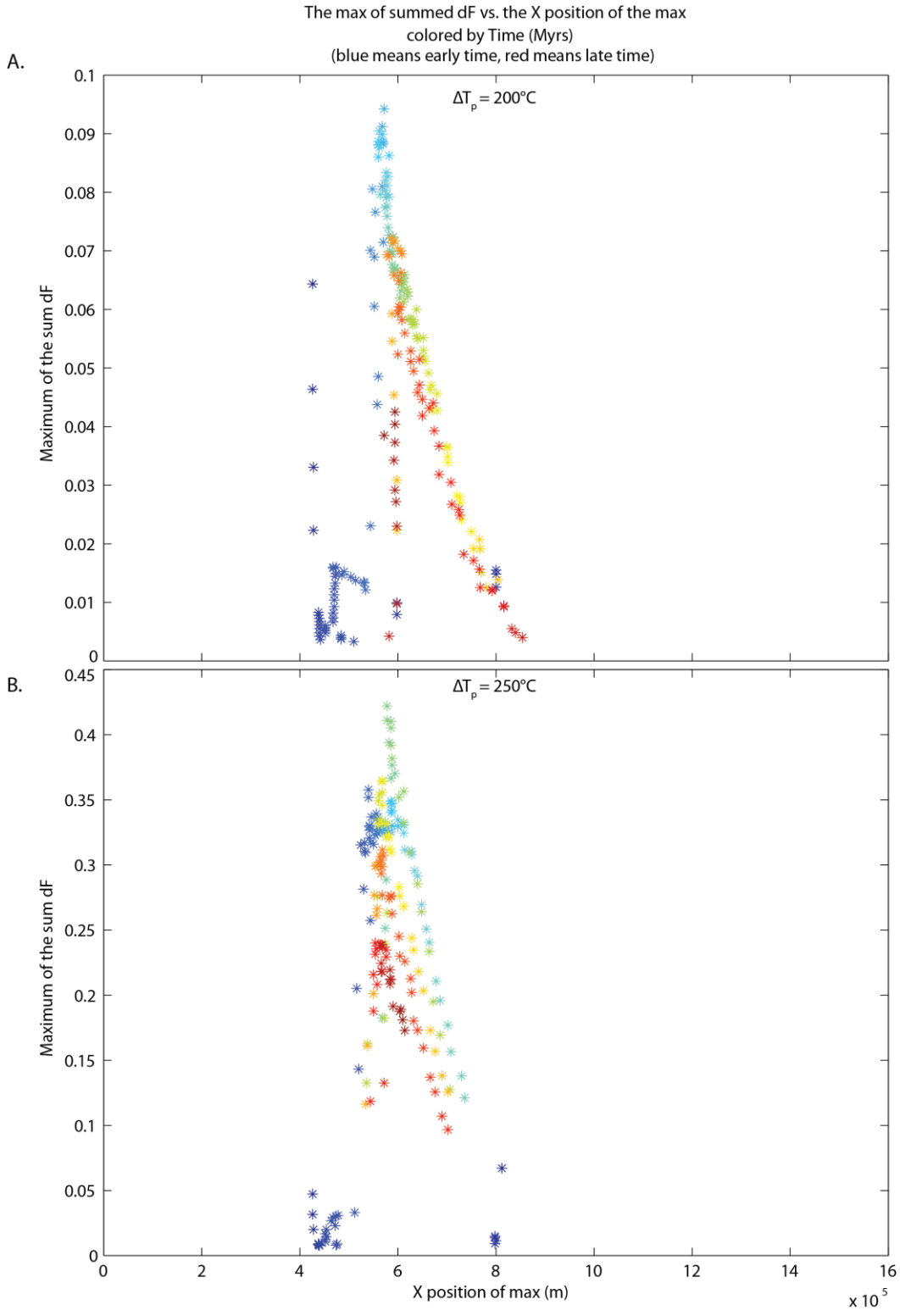
The max of summed dF vs. the X position of the max
colored by Time (Myrs)
(blue means early time, red means late time)
A.
ΔT_p = 200°C
Maximum of the sum dF
0.1
0.09
0.08
0.07
0.06
0.05
0.04
0.03
0.02
0.01
0
B.
ΔT_p = 250°C
Maximum of the sum dF
0.45
0.4
0.35
0.3
0.25
0.2
0.15
0.1
0.05
0
0
2
4
6
8
10
12
14
16
X position of max (m)
x 10^5

Figure 14

Figure 14. Maximum integrated instantaneous melting (*dF*) vs. X-position within the model domain (m) is shown for Experiments 3-4. The colors reflect time in Myr, ranging from 0 Myr (blue) to 20 Myr (red). **A.** Depiction of Experiment 3, with ΔT_p = 200 °C. Peak melting activity occurs at ~600 km approximately halfway through the run-period of 20 Myr. The position of the maximum melting activity migrates, reaching ~850 km by the end of the run. **B.** Plot for Experiment 4 for ΔT_p = 250 °C. Peak melting activity occurs at nearly the same position, 600 km, as it does in **A**. The position of peak melting activity fluctuates, and does seem to migrate further within the model domain, but the maximum melting does not extend past ~800 km. The 50 °C increase between **A** and **B** seems to decrease the extent to which the maximum melting activity is occurring, contrary to the relationship shown in Figure 13. Peak melting activity in **A** and **B** returns back to ~550-600 km, but is more pronounced in **B**. The fluctuations in position reflect the waves propagating at ~550-600 km, and show the difference in the amount of waves created by the different values of ΔT_p.

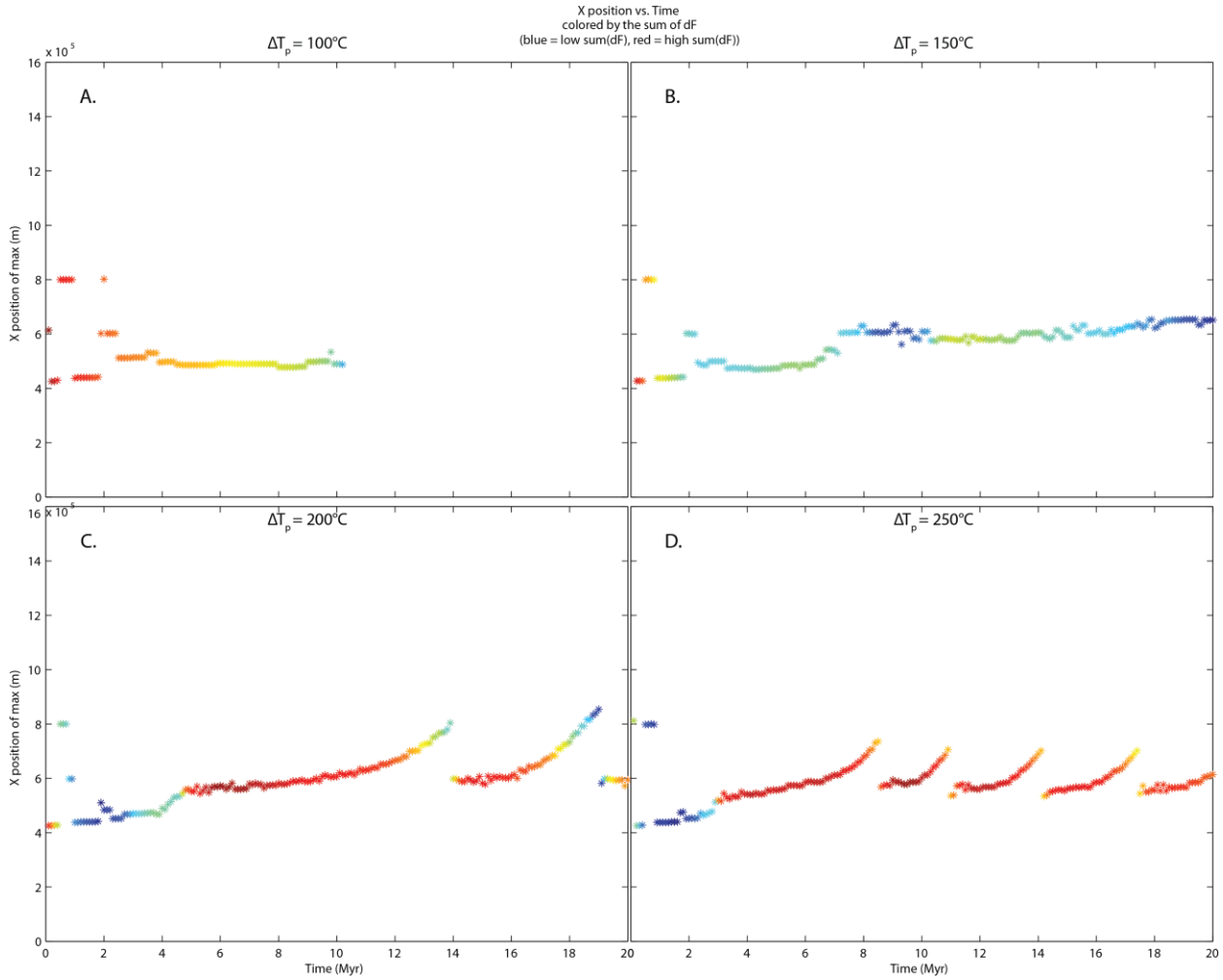

Figure 15. X-position vs. Time (Myr) for Experiments 1-4, which vary ΔT_p. The colors of the points represent maximum integrated instantaneous melt (*dF*), or maximum melt activity, with red indicating the highest melting activity within each experiment and blue representing the lowest melting activity. Figures 9-14 provide explanations of the observed trends and differences for these experiments. From **A** to **B**, increasing ΔT_p by 50 °C prolongs the duration of melting activity by 9-9.5 Myr. In **B**, and continuing in **C** and **D**, the amount of melting fluctuates from higher to lower values, and forms a sequence that increases in repetitions with increasing temperature. In **C** and **D**, melting activity fluctuates within a tighter range of values that is significantly higher relative to **B**. Additionally, the changes in

position in **C** and **D** reflect the waves that begin to propagate after the plume has moved beyond the discontinuity at 400 km. As is visible in Figure 14, more waves are generated and wave propagation begins earlier in Experiment 4 (ΔT_p = 250 °C) than in Experiment 3 (ΔT_p = 200 °C). The spatial and temporal differences in melting activity in Experiments 1-4 reflect the sensitivity of the model to fluctuations of ΔT_p, and show that if ΔT_p is high enough, the effect of time on thickness of the thermal boundary layer (per HSC) is diminished.

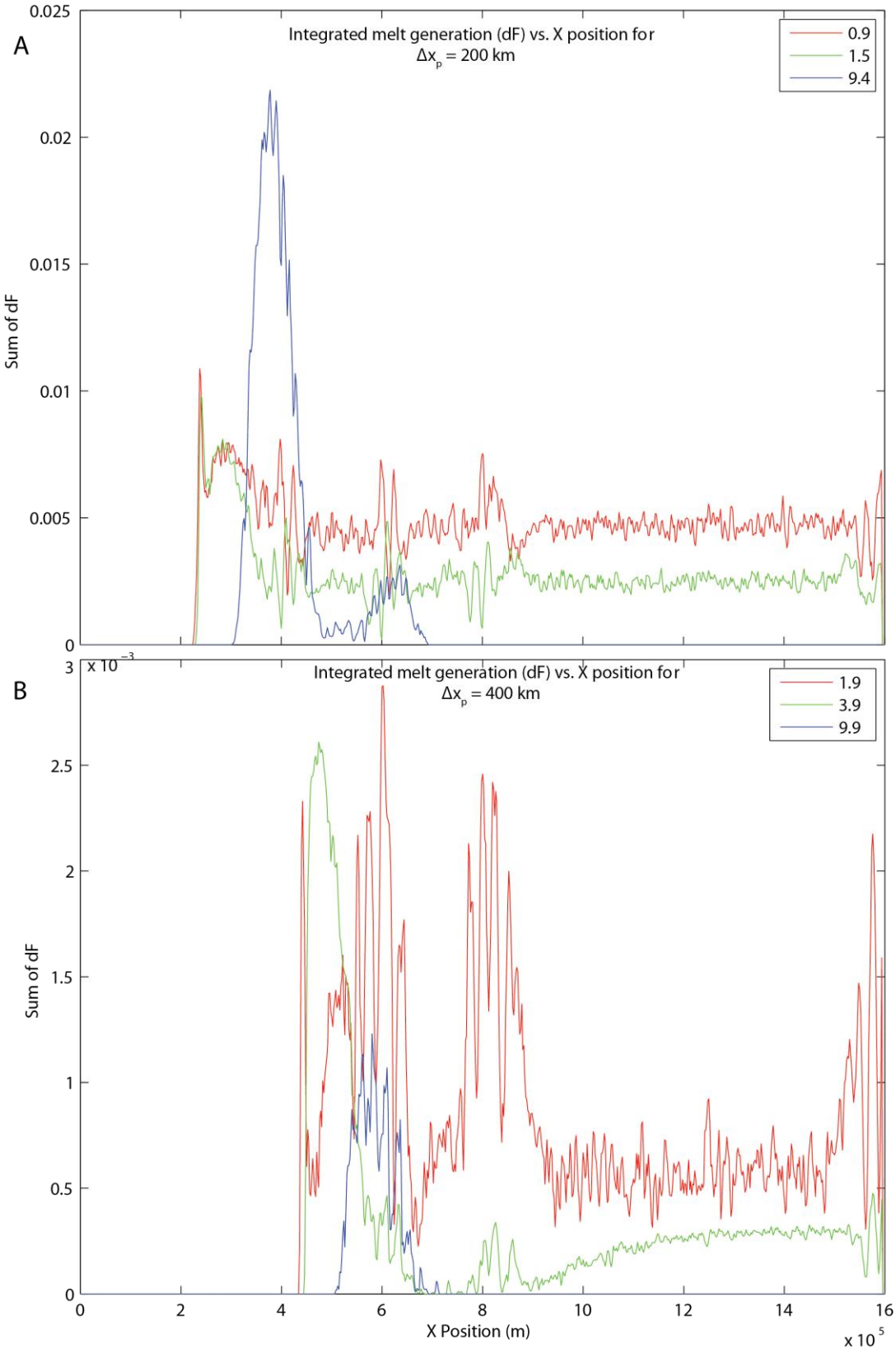
A
Integrated melt generation (dF) vs. X position for
Δx_p = 200 km
0.9
1.5
9.4
Sum of dF
0.025
0.02
0.015
0.01
0.005
0
x 10^-3
B
Integrated melt generation (dF) vs. X position for
Δx_p = 400 km
1.9
3.9
9.9
Sum of dF
3
2.5
2
1.5
1
0.5
0
0
2
4
6
8
10
12
14
16
X Position (m)
x 10^5

Figure 16

Figure 16. Melt generation (*dF*) integrated over depth and plotted vs. X-position (m) in the modeling domain for Experiments 5 and 1 (reference experiment), which vary the distance between the plume and the transform boundary (Δx_p). The sum, or integral of *dF*, is plotted for three times during the period of 20 Myr, depicting conditions before the plume has reached the discontinuity, when the plume has arrived at it, and after the plume has crossed and continued onward. **A.** Integrated *dF* for Δx_p = 200 km at 0.9, 1.5, and 9.4 Myr. Of the times depicted, the least melt is generated at the plume's arrival at the transform boundary. The peak melt generation occurs after the plume has moved beyond the discontinuity at 200 km, and occurs at a distance between 300 and 500 km. The location of the highest melting activity moves further away from the plate boundary at 200 km as the plume makes its way to and across it. **B.** Integrated *dF* for reference conditions, with Δx_p = 400 km at 1.9, 3.9, and 9.9 Myr. See Figure 9B for a description. The change of 200 km in Δx_p between **A** and **B** is enough to alter when peak melting activity occurs relative to the lateral progression of the plume through the model domain.

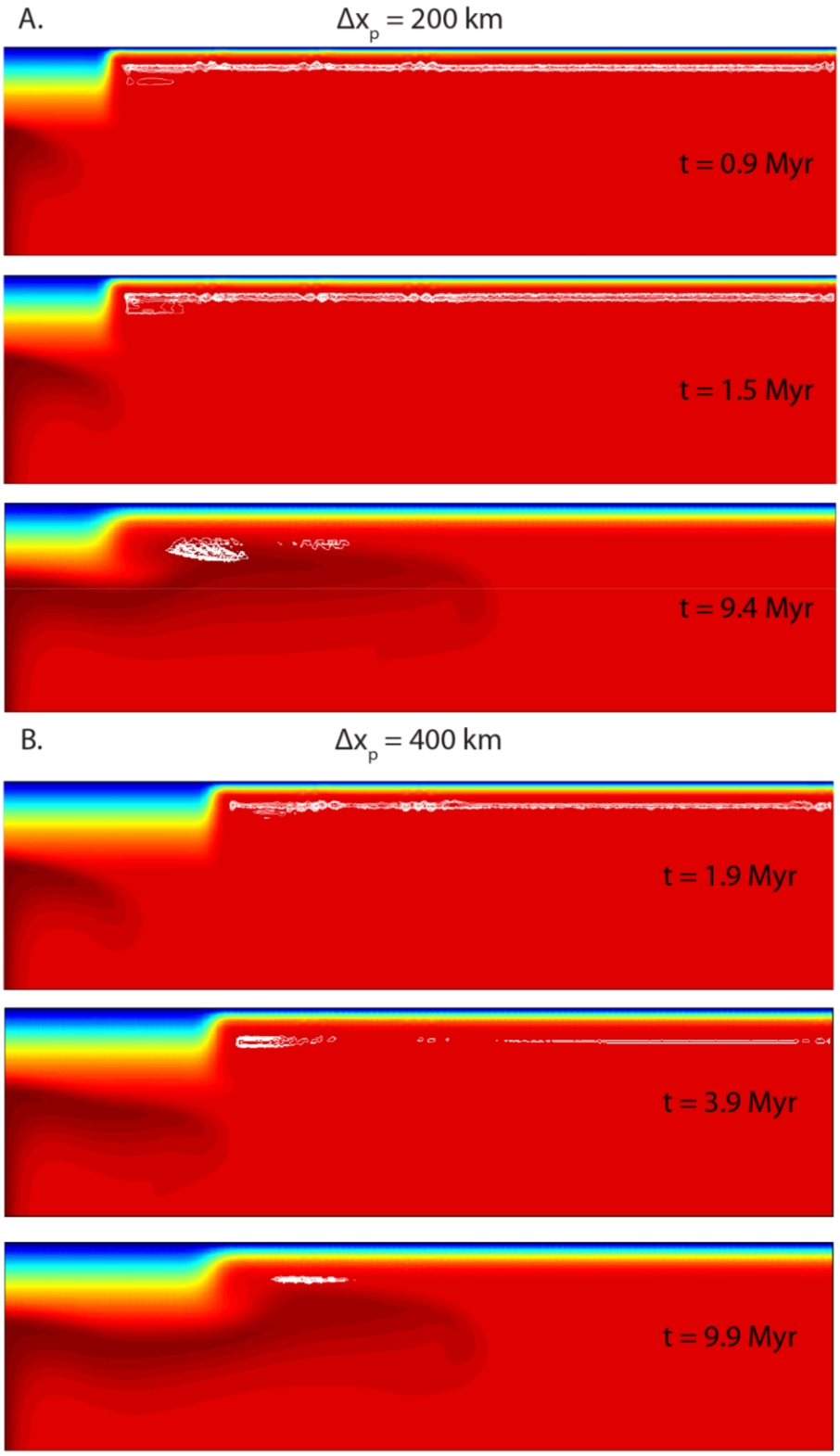
A.
Δx_p = 200 km
t = 0.9 Myr
t = 1.5 Myr
t = 9.4 Myr
B.
Δx_p = 400 km
t = 1.9 Myr
t = 3.9 Myr
t = 9.9 Myr

Figure 17.

Figure 17. Snapshots of the temperature fields for Experiments 5 and 1 corresponding to the experiments and times shown in Figure 16. Instantaneous melt generation (*dF*) is displayed as white contours. **A.** Snapshots of the temperature fields for Experiment 5 with Δx_p = 200 km at 0.9, 1.5, and 9.4 Myr. As shown in Figure 16A, the peak melt generation occurs after the plume has moved beyond the discontinuity at 200 km, at a distance between ~300 and ~500 km. The location of the highest melting activity moves further away from the plate boundary at 200 km as the plume makes its way across it. **B.** Snapshots of the temperature fields for Experiment 1, depicting reference conditions, with Δx_p = 400 km at 1.9, 3.9, and 9.9 Myr. See Figure 10B for description of Experiment 1.

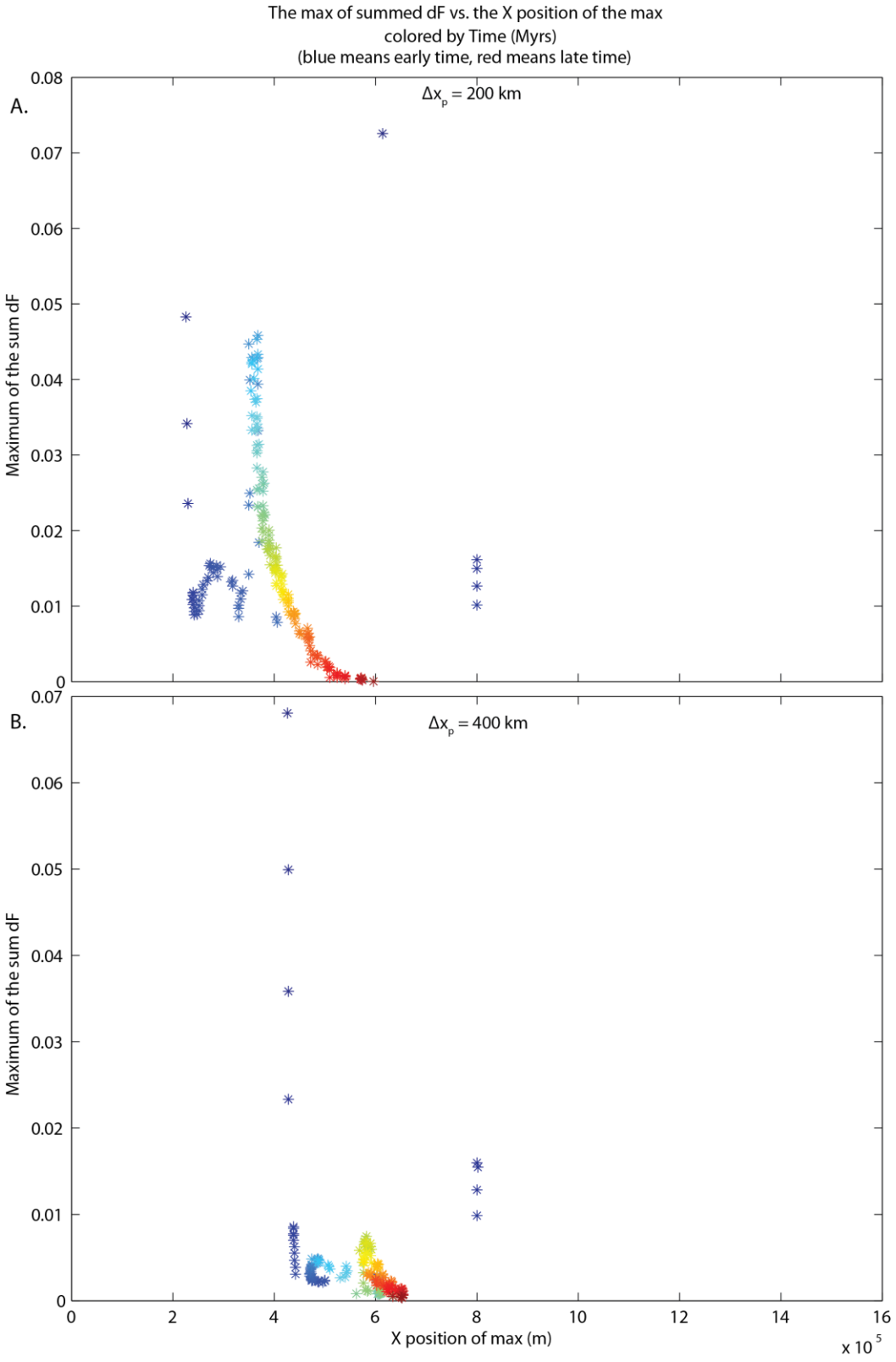
The max of summed dF vs. the X position of the max
colored by Time (Myrs)
(blue means early time, red means late time)
A.
Δx_p = 200 km
B.
Δx_p = 400 km
Maximum of the sum dF
X position of max (m)
x 10^5
0
0.01
0.02
0.03
0.04
0.05
0.06
0.07
0.08
2
4
6
8
10
12
14
16

Figure 18

Figure 18. Maximum values of the integration of instantaneous melt generation (*dF*) vs. x-position within the model domain (m) is shown for Experiments 5 and 1. The colors reflect time in Myr, ranging from 0 Myr (blue) to 20 Myr (red). **A.** Depiction of Experiment 5, with Δx_p = 200 km. The short distance between the plume and the discontinuity shortens the time it takes for the plume to reach and pass the plate boundary. In Figures 16A and 17A, the peak integrated instantaneous melting occurred after the plume had passed the discontinuity; however, it is evident here that the highest maximum value of integrated *dF* occurs before the plume has even reached the discontinuity at 200 km. **B.** Plot for the reference conditions (Exp. 1, Table 2) where Δx_p = 400 km. See Figure 11B for analysis. In **A**, there is a wider range on the x-axis over which the maximum values of integrated *dF* occur than in **B** because, with Δx_p = 200 km, the shorter distance decreases the time taken for the plume to cross the discontinuity. This means that the plume encounters a younger plate than it does when it crosses the discontinuity in **B**. Because the young plate is younger in **A**, the thermal boundary is thinner, and melting may occur more readily at shallower depths than in **B**.

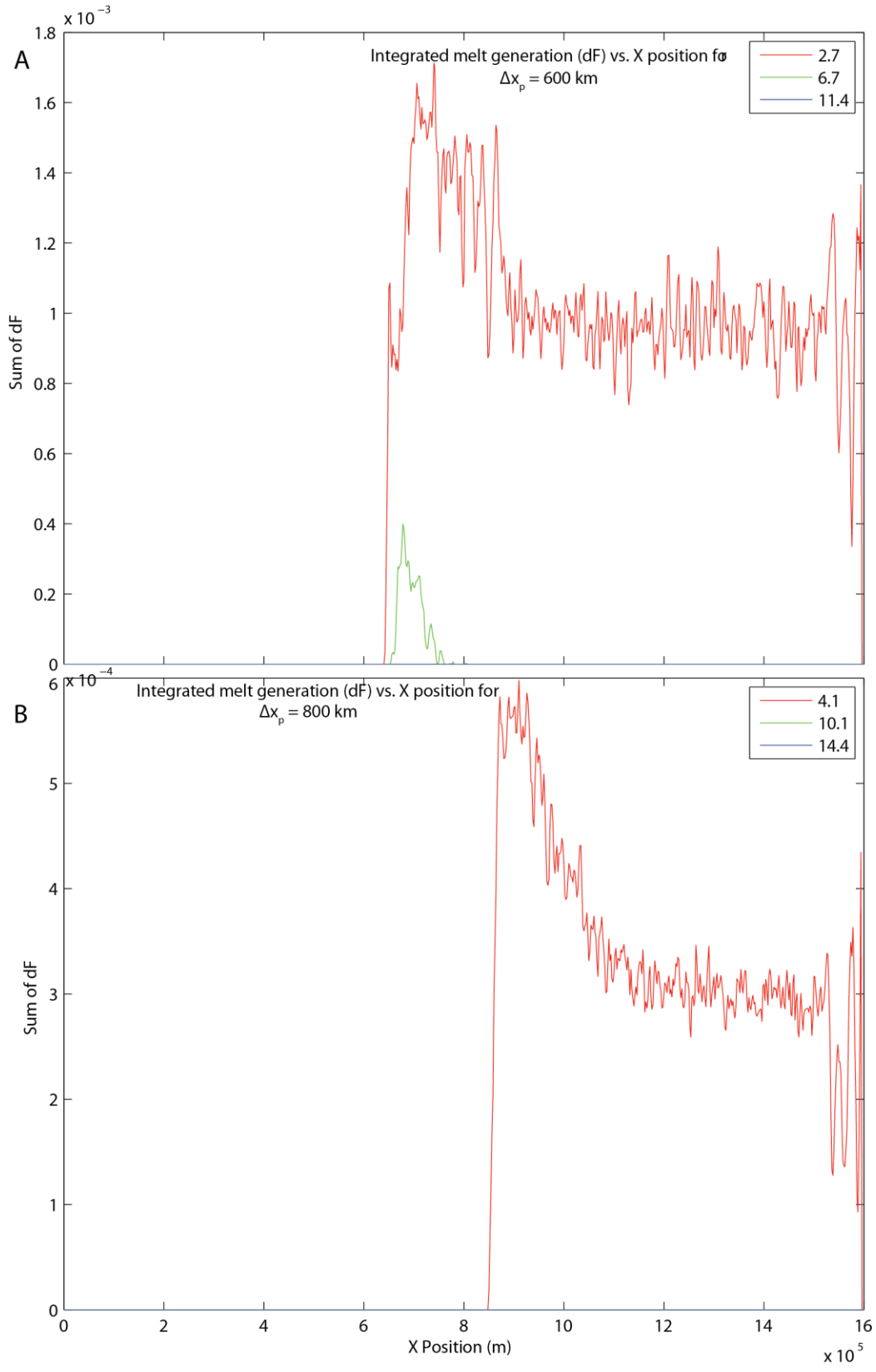
A
x 10^-3
Integrated melt generation (dF) vs. X position fo
Δx_p = 600 km
2.7
6.7
11.4
Sum of dF
B
x 10^-4
Integrated melt generation (dF) vs. X position for
Δx_p = 800 km
4.1
10.1
14.4
Sum of dF
X Position (m)
x 10^5

Figure 19

Figure 19. Melt generation (*dF*) integrated over depth and plotted vs. x-position (m) in the modeling domain for Experiments 6-7, which vary the distance between the plume and the transform boundary (Δx_p). The sum, or integral of *dF* is plotted for three times during the period of 20 Myr, depicting conditions: (1) before the plume has reached the discontinuity, (2) when the plume has arrived at it, and (3) after the plume has crossed and continued onward. **A.** Integrated *dF* for Δx_p = 600 km at 2.7, 6.7, and 11.4 Myr. Of the times depicted, the least melting activity occurs at 6.7 Myr, which corresponds to the plume's arrival at the transform boundary, and is limited to the area in the domain from ~650 km to ~775 km. The peak melting activity occurs before the plume has moved beyond the discontinuity (600 km) at ~630 km and continues to ~900 km, although the melting activity is fairly uniform. A curve is not shown for 11.4 Myr when the plume has crossed the discontinuity and continued onwards, because melting does not occur. **B.** Integrated *dF* for Experiment 7, with Δx_p = 800 km at 4.1, 10.1, and 14.4 Myr. Of the times chosen, melting only occurs before the plume has reached the discontinuity. Melting starts at ~850 km as mantle material ahead of the plume is pushed to lower depths and pressures and undergoes decompression melting. **A** and **B** show that with a distance of 600-800 km between the plume and the discontinuity, melting activity cannot persist for the full period of 20 Myr.

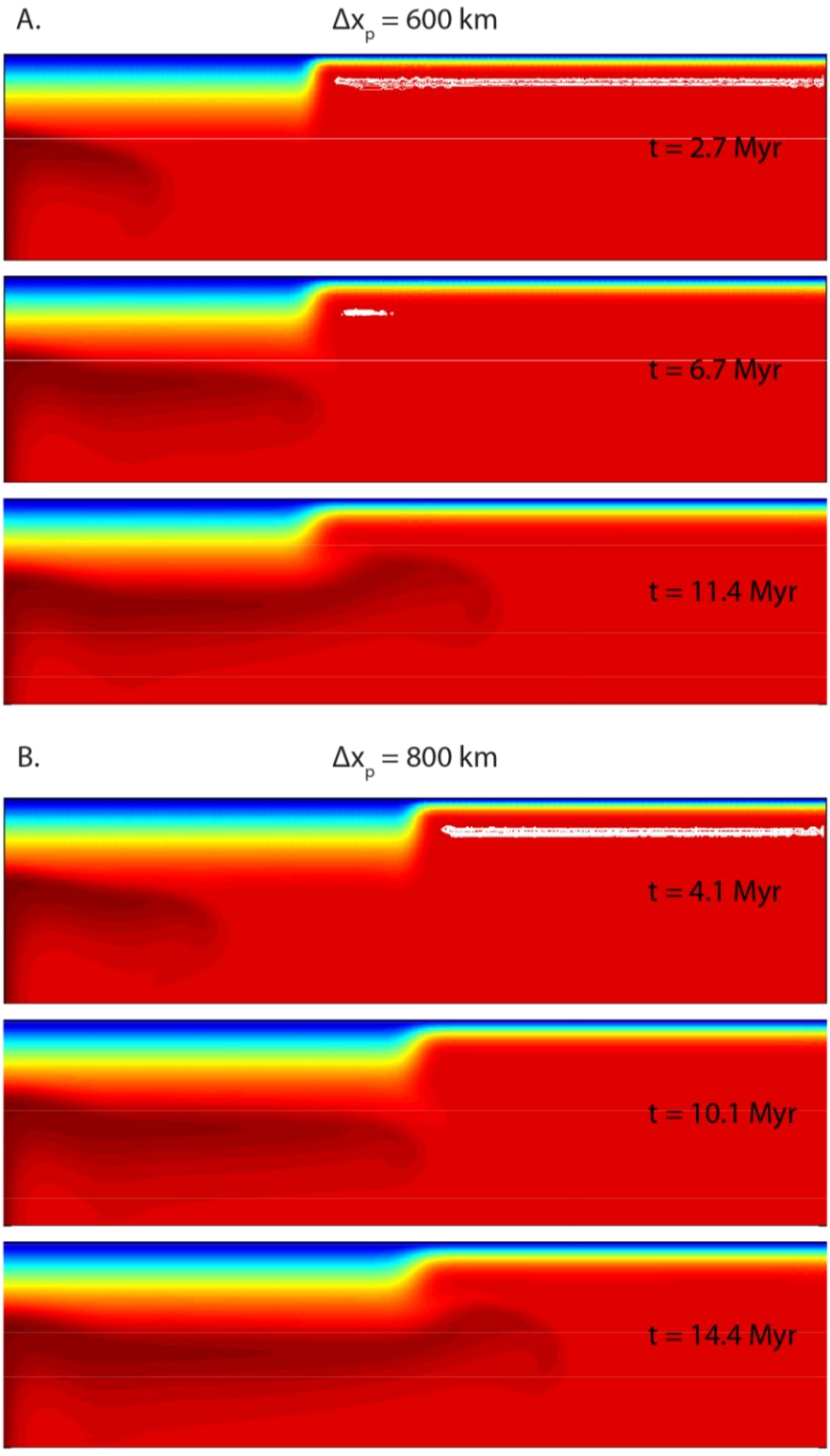
A.
Δx_p = 600 km
t = 2.7 Myr
t = 6.7 Myr
t = 11.4 Myr
B.
Δx_p = 800 km
t = 4.1 Myr
t = 10.1 Myr
t = 14.4 Myr

Figure 20

Figure 20. Snapshots of the temperature fields for Experiments 6-7 corresponding to the experiments and times shown in Figure 19. Instantaneous melt generation (*dF*) is displayed as white contours. **A.** Snapshots of the temperature fields for Experiment 6 with Δx_p = 600 km at 2.7, 6.7, and 11.4 Myr. As shown in Figure 19A, peak melt generation occurs before the plume has reached the discontinuity at 600 km. Melting activity is diminished and less widespread once the plume has arrived at the transform boundary, and melting does not occur after it has crossed and continued through the domain. **B.** Snapshots of the temperature fields for Experiment 7 with Δx_p = 800 km at 4.1, 10.1, and 14.4 Myr. Just as in Figure 19B, melting only occurs before the plume reaches the discontinuity at 800 km. In both **A** and **B**, melting activity ceases before the time period of 20 Myr because the transform boundary is so far away from the plume. The increased distance (compared to 200 km and 400 km in Experiments 5 and 1) makes the plume travel further beneath the thicker plate and increases the time it takes to reach the discontinuity. By the time the plume does reach the discontinuity, the younger plate has aged such that it has developed a thicker thermal boundary, and melting is either diminished (as in **A**) or is unable to occur (as in **B**).

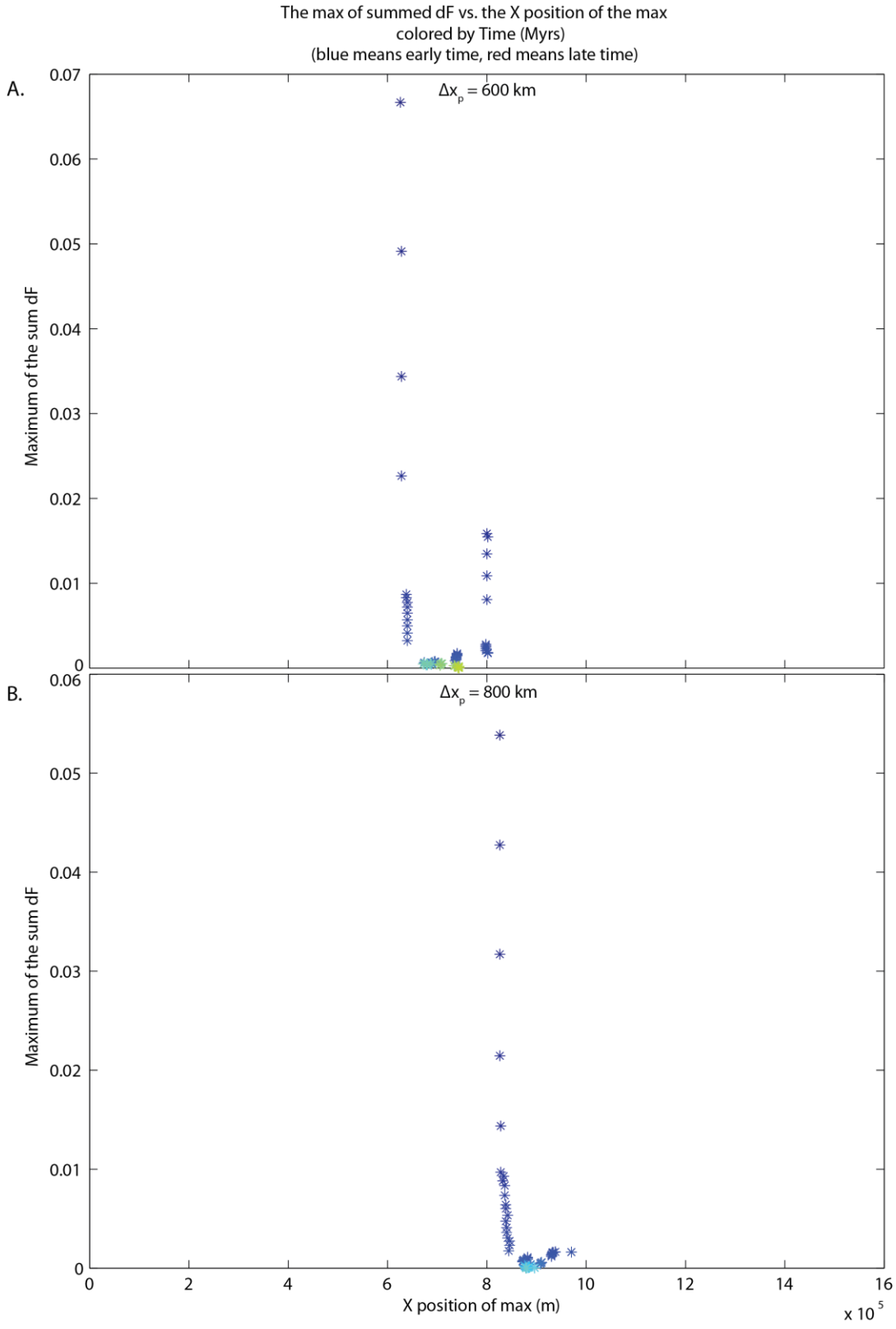
The max of summed dF vs. the X position of the max
colored by Time (Myrs)
(blue means early time, red means late time)
A.
Δx_p = 600 km
Maximum of the sum dF
0.07
0.06
0.05
0.04
0.03
0.02
0.01
0
B.
Δx_p = 800 km
Maximum of the sum dF
0.06
0.05
0.04
0.03
0.02
0.01
0
0
2
4
6
8
10
12
14
16
X position of max (m)
x 10^5

Figure 21

Figure 21. Maximum integrated instantaneous melting (*dF*) vs. x-position within the model domain (m) is shown for Experiments 6-7. The colors reflect time in Myr, ranging from 0 Myr (blue) to 20 Myr (red). **A.** Depiction of Experiment 6, with Δx_p = 600 km. As shown in Figures 19A and 20A, melting in Experiment 2 does not persist for the full period of 20 Myr—shown here by the absence of colors corresponding to the latter ~8 Myr. Aside from the high maximum integrated *dF* values that occur for all experiments with the onset of the plume, melting activity is very uniform. **B.** Plot for Experiment 7 for Δx_p = 800 km. Just as shown in Figures 19B and 20B, melting activity only occurs prior to the arrival of the plume at the discontinuity because the younger plate has aged so much by the time the plume has reached it and crossed, that the thermal boundary is too thick to allow adiabatic decompression melting to persist. Both **A** and **B** show that if the distance between the plume and the transform boundary is increased to 600 km or more, the progress of the plume is slowed to such an extent that decompression melting becomes unfeasible.

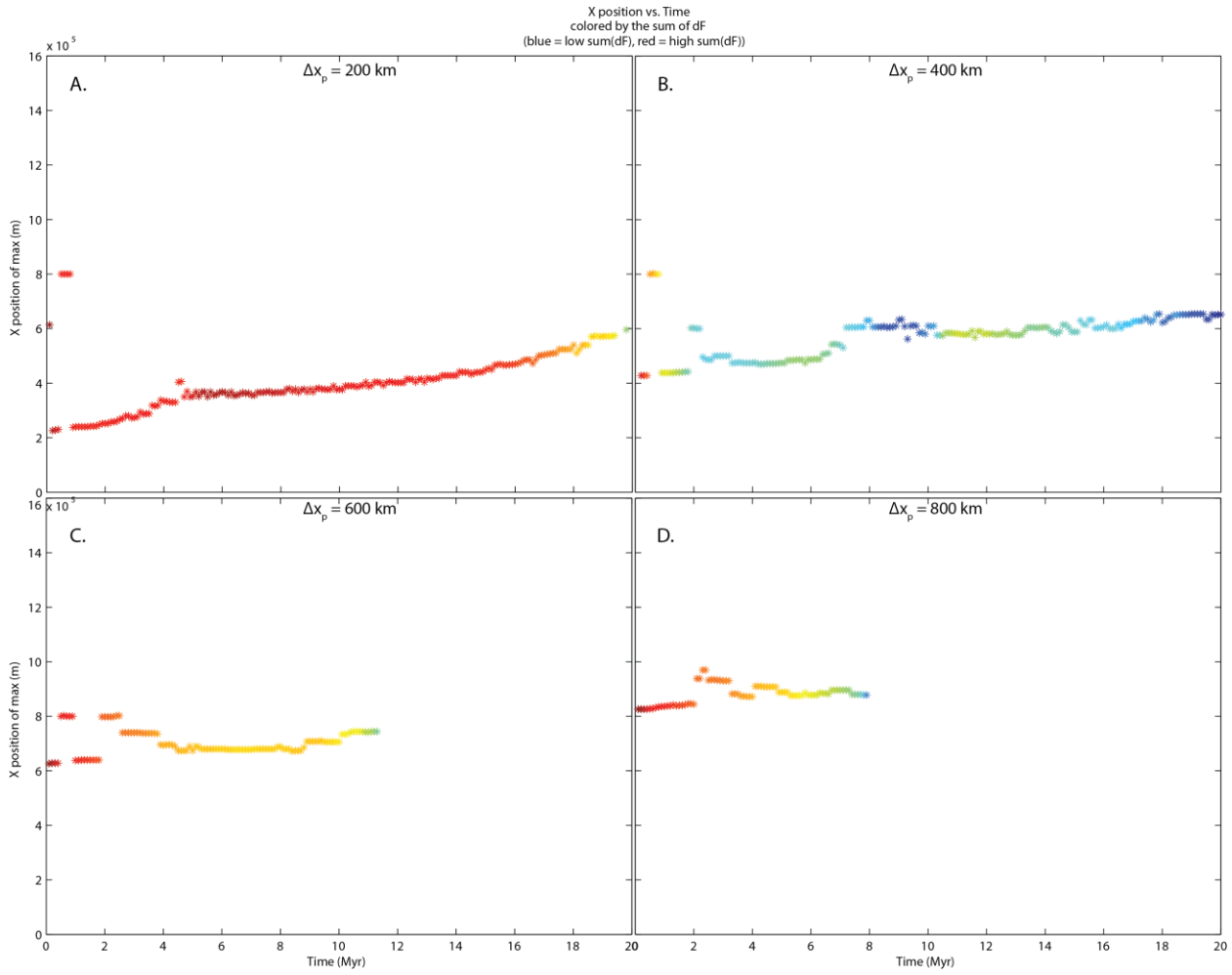

Figure 22. X-position is plotted vs. Time (Myr) for Experiments 1, 5-7, which vary Δx_p. The colors of the points represent maximum integrated instantaneous melt (*dF*), or maximum melt activity, with red indicating the highest melting activity within each experiment and blue representing the lowest melting activity. Figures 16-21 provide explanation of observed trends and differences for the experiments varying Δx_p shown here. For each of the experiments represented by **A**-**D**, Δx_p is 200 km higher than in the previous experiment, beginning at 200 km for **A**. With increasing Δx_p, the lateral range in position over which maximum integrated *dF* occurs decreases, and at $\Delta x_p \geq 600$ km in **C** and **D**, melting no longer persists for the 20 Myr duration. The spatial and temporal differences in melting activity in Experiments 1 and 5-7 reflect the sensitivity of the model to changes in Δx_p, and show that

Δx_p relates directly to age and its effect on lithospheric thickness. Increasing the distance between the plume and the discontinuity causes the plume to reach the "younger plate" when it has aged to the point that the thermal boundary of the plate has grown very thick (per HSC), stifling any decompression melting from occurring.

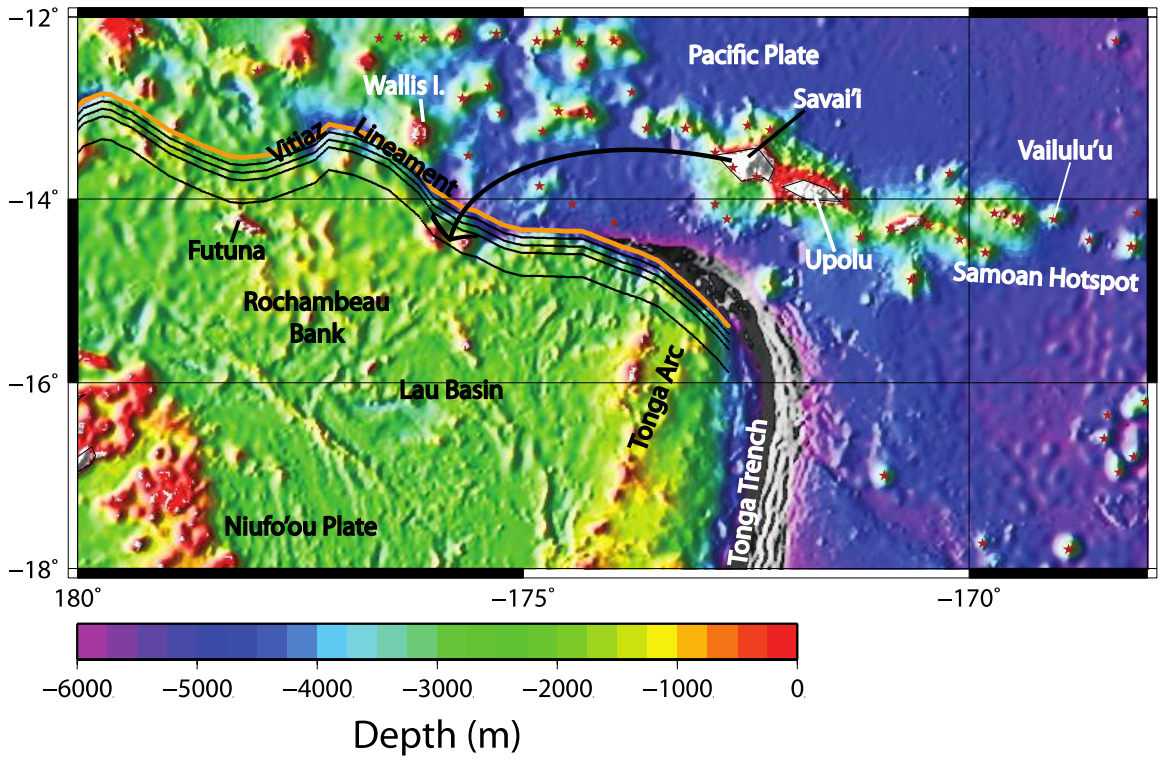

A. ★ = Seamount identified by Wessel and Kim (2010)

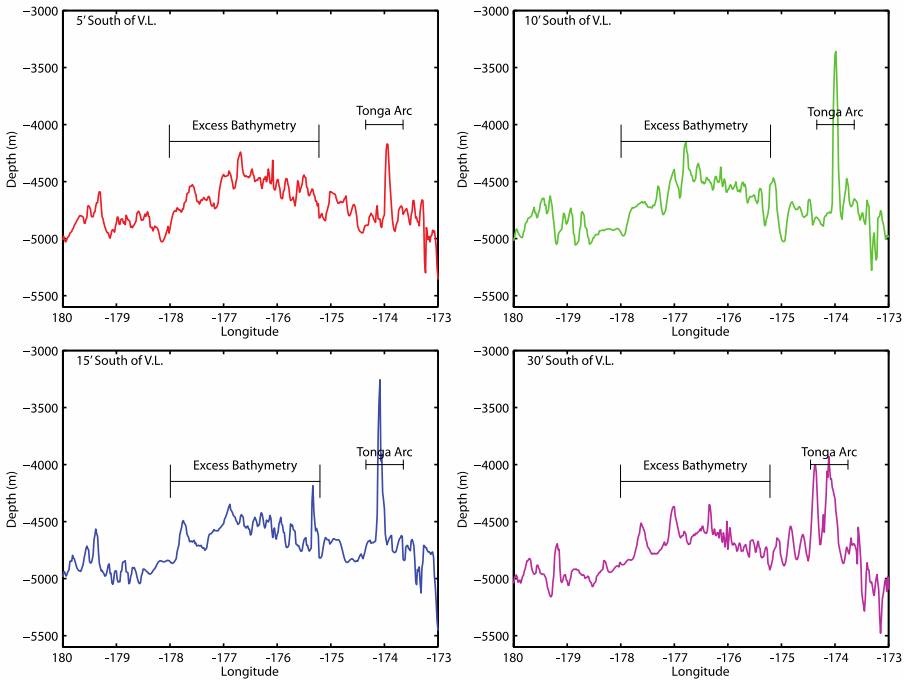

B.

Figure 23

Figure 23. ETOPO1 bathymetry of the northern Lau basin. Along the Vitiaz lineament (orange line), regions with pronounced intervals of bathymetric highs are considered to have excess bathymetry, which can be used as a proxy for excess volcanism. **A**. Bathymetric map of the northern Lau basin. The black lines running east-west, parallel to the Vitiaz lineament, correspond to the graphs in **B**. **B**. Graphs of depth vs. longitude along transects at 5 ‘, 10’, 15’, and 30’ south of the lineament (solid black lines marked in **A)**. There is a noticeable increase in sea floor elevation, or excess bathymetry, between ~178° W and ~175° W, corresponding to several sea mounts parallel to the Vitiaz lineament (orange line). This increase in elevation persists past 30’ south of the lineament. The interval spanning from ~178° W and ~175° W is proposed to indicate the point of entry for the Samoan-plume mantle.